Enhanced upwelling of Antarctic Bottom Water by topographic interaction of water mass interfaces

L. E. Baker[1], A. Mashayek[1], A. C. Naveira Garabato[2]

[1]Imperial College London, United Kingdom
[2]University of Southampton, Southampton, United Kingdom

Key Points:

- Sharp density interfaces exist between Antarctic Bottom Water and overlying Circumpolar Deep Water in the Drake Passage
- The sharpness of the interfaces leads to rich submesoscale and internal wave dynamics and complex topographic interactions
- Such dynamics may contribute significantly to upwelling of Antarctic Bottom Water

Corresponding author: Lois Baker, l.baker18@imperial.ac.uk

Abstract

The lower cell of the meridional overturning circulation (MOC) is sourced by dense Antarctic Bottom Water (AABW), which forms and sinks around Antarctica and subsequently fills the abyssal ocean. For the MOC to 'overturn', these dense waters must upwell through mixing with lighter waters above. Here, we investigate the processes underpinning such mixing, and the resulting water mass transformation, using an observationally forced, high-resolution numerical model of the Drake Passage in the Southern Ocean. In the Drake Passage, the mixing of dense AABW formed in the Weddell Sea with lighter deep waters transported from the Pacific Ocean by the Antarctic Circumpolar Current is catalysed by energetic flows impinging on rough topography. We find that multiple topographic interaction processes act to facilitate mixing of the two water masses, ultimately resulting in upwelling of waters with neutral density greater 28.19 kg m^{-3}, and downwelling of the lighter waters above. In particular, we identify the role of sharp density interfaces between AABW and overlying waters, and find that the dynamics of the interfaces' interaction with topography can enhance mixing. Such sharp interfaces between water masses have been observed in several parts of the global ocean, but are unresolved and unrepresented in ocean and climate models. We suggest that they are likely to play an important role in abyssal dynamics and mixing, and therefore require further exploration.

Plain Language Summary

Dense, cold waters are formed near Antarctica, then sink and spread through the deep ocean. The global overturning circulation is maintained by the upwelling of these dense waters back to the surface. This circulation allows the abyssal ocean to exchange heat, carbon and other tracers with the upper ocean and atmosphere, and is therefore a key regulator of the climate system. The upwelling happens due to turbulence in the deep ocean mixing together dense waters with lighter waters above. This turbulent mixing is often caused by the interaction of currents with rough seafloor topography, but the processes and resulting upwelling are not well understood. In this study, we use a high-resolution, realistic numerical simulation to investigate the processes causing turbulent mixing and upwelling of dense waters in an energetic region of the Southern Ocean. We find that there are sharp interfaces between the Antarctic-sourced dense waters and the overlying lighter waters, and that these interfaces themselves play a dynamic role in generating turbulent mixing and upwelling. The interfaces are not resolved or represented in global climate models, so their impact on the deep-ocean circulation requires further exploration.

1 Introduction

Sea ice formation and surface cooling near Antarctica create the densest waters in the global ocean (Marshall & Speer, 2012; Talley, 2013; A. C. Naveira Garabato et al., 2014). These Antarctic Bottom Waters (AABW) sink and travel northwards below the lighter water masses, filling most of the abyssal ocean with dense, cold, relatively fresh water (Lumpkin & Speer, 2007; Johnson, 2008; Talley, 2013). Such formation of AABW feeds the lower cell of the meridional overturning circulation (MOC). For these waters to upwell back to the surface (for if they did not, the ocean would fill up with dense waters), they must first upwell across density surfaces by transforming diabatically to lighter waters. Once they are sufficiently light, they then enter the upper cell of the MOC, where they are drawn adiabatically to the surface by westerly winds in the Southern Ocean (Toggweiler, 1994; Marshall & Speer, 2012; Talley, 2013). This overturning circulation ventilates the ocean abyss on timescales of centuries to millennia, with leading-order climatic consequences for the deep-ocean storage and release of carbon, heat and other tracers (Talley, 2013; Rae et al., 2018; Skinner et al., 2010).

The primary mechanism by which AABW can upwell across density surfaces is thought to be turbulent diapycnal mixing (Munk & Wunsch, 1998; Wunsch & Ferrari, 2004; De

Lavergne et al., 2016; Meredith & Naveira Garabato, 2021), the other non-negligible (yet secondary) mechanism being geothermal heating (Emile-Geay & Madec, 2009; Mashayek et al., 2013; Mashayek, Salehipour, et al., 2017; De Lavergne et al., 2016; Cimoli et al., 2019). Turbulent diapycnal mixing in the ocean occurs when small-scale turbulence causes irreversible mixing of fluids with different densities. Observations show that this turbulent mixing is enhanced by several orders of magnitude within a few hundred metres of the seafloor, compared to at mid-depths (Polzin et al., 1997; Ledwell et al., 2000; A. Naveira Garabato et al., 2004; J. MacKinnon et al., 2013; Waterhouse et al., 2014; J. A. MacKinnon et al., 2017). This is due to turbulent processes generated by the interaction of currents and tides with topography at the sea floor. These processes include internal waves, which are thought to be a primary source of mixing in the ocean interior (Wunsch & Ferrari, 2004; J. A. MacKinnon et al., 2017; Sarkar & Scotti, 2017; Whalen et al., 2020), and other non-propagating boundary dynamics such as hydraulic processes (Baines, 1995; Legg & Klymak, 2008; Alford et al., 2013; Klymak, 2018) and Ekman layers (Garrett et al., 1993; A. C. Naveira Garabato et al., 2019; Spingys et al., 2021).

However, the implication of turbulent processes being bottom-generated is that the turbulent diffusivity increases towards topography, which induces downwelling rather than upwelling across density surfaces (Polzin et al., 1997; L. C. St. Laurent et al., 2001; De Lavergne et al., 2016; Ferrari et al., 2016). This apparent conundrum can be resolved by realising that, in some boundary layer next to topography, waters cannot become denser, and so must become lighter by mixing with waters above them, thereby inducing upwelling (Ferrari et al., 2016; McDougall & Ferrari, 2017). In recent years, there has been a significant focus on the nature of diapycnal mixing and density stratification in the bottom boundary layer, due to its key role in facilitating upwelling of dense waters, as reviewed by Polzin and McDougall (2022). The processes through which near-boundary waters mix, re-stratify and are exchanged with the ocean interior, and how those processes vary geographically throughout the global ocean, are a key open question.

The difficulty in answering this question resides in the extreme challenge involved in observing turbulence in the abyssal ocean, particularly close to the seafloor. From a modelling perspective, high-resolution, process-resolving numerical simulations must be idealised and small-scale due to computational limitations, while more realistic simulations lack accurate parameterizations for mixing processes below the grid-scale. In this study, we use a realistic, wave- and submesoscale-resolving simulation to shed light onto the abyssal processes that generate mixing and drive transformation of AABW, as this water mass flows northwards through the Southern Ocean. We choose to study the Drake Passage, a region of intense flow-topography interaction and diapycnal mixing.

The Drake Passage is the gap between the tip of South America and the Antarctic Peninsula, through which the energetic Antarctic Circumpolar Current (ACC) flows from west to east. Rough topography including ridges, seamounts and abyssal hills (see figures 1b,d) obstructs the deep layers of the ACC, generating intense diapycnal mixing in the bottom 1-2 km (A. Naveira Garabato et al., 2004; L. St. Laurent et al., 2012; Sheen et al., 2013; Mashayek, Ferrari, et al., 2017; Mackay et al., 2018). It is thought that the main contributor to mixing at depth in the Drake Passage is the breaking of internal lee waves generated by the impingement of the vigorous mesoscale eddies of the ACC upon the rough topography (L. St. Laurent et al., 2012; Sheen et al., 2013; Nikurashin & Ferrari, 2010), although the ways in which lee waves lose energy to diapycnal mixing are still not well understood (Legg, 2021).

The impact of concentrated 'hotspots' of topographic mixing, such as the Drake Passage, on global deep-water upwelling has long been recognised (Munk & Wunsch, 1998). In addition, increased tracer residence time near large-scale ridges and fracture zones has been shown to contribute to enhanced diapycnal tracer transport in the Drake Passage (Mashayek, Ferrari, et al., 2017). This makes the Drake Passage an important location, not

only for transformation of dense bottom waters, but also for upwelling of climate-critical tracers such as heat, carbon and nutrients (Tamsitt et al., 2017).

The singular role of the Drake Passage in mixing AABW is partly due to its location. It is on the northward path of the dense AABW that is formed in the Weddell Sea to the south, called Weddell Sea Deep Water (Sievers & Nowlin, 1984; A. C. Naveira Garabato, Heywood, & Stevens, 2002, hereafter, NG02a). In the Drake Passage, Lower Circumpolar Deep Water (LCDW) sits above AABW, having entered the passage from the Pacific Ocean to the west. AABW occupies only the south-east part of the Passage (NG02a), so the AABW/LCDW interface directly impinges on the rough Drake Passage topography, experiencing high levels of topographically enhanced turbulent diapycnal mixing as a result. However, the processes by which the mixing at this interface takes place are not well understood. Furthermore, the boundary layer adjacent to topography in which diapycnal upwelling is expected to happen exists over a wide range of depths in the Passage, so it is not clear which density classes can be expected to upwell, and which may instead downwell.

Here, we investigate how flow-topography interaction processes in the Drake Passage act to mix AABW with the overlying LCDW, and quantify the resulting water mass transformation. Although the Drake Passage is an energetic region, AABW export and northward transport occur in every major ocean basin, so it is expected that the dynamics described here are not unique, and could be of more generic importance to the transformation of AABW as it navigates the ACC and rough topography of the Southern Ocean.

2 Drake Passage Simulation

We use a wave-resolving model of the Drake Passage, described in detail in Baker and Mashayek (2022) (see Appendix A for summary). The simulation is performed using the hydrostatic configuration of the Massachusetts Institute of Technology general circulation model (MITgcm, Marshall et al., 1997), with 0.01° horizontal resolution (600 m to 1100 m) and 225 vertical levels with variable resolution that is < 25 m at all depths above -4500 m (the range of depths relevant to this work). The depth and main bathymetric features are shown in figure 1d. Figure 1b shows a daily average of vertical vorticity in the simulation domain, demonstrating the interaction of deep-reaching mesoscale eddies with the rough topography.

The simulation is based upon a similar simulation that was developed as part of the DIMES (Diapycnal and Isopycnal Mixing Experiment in the Southern Ocean) field programme (Mashayek, Ferrari, et al., 2017). The DIMES experiment included a release in 2009 of an anthropogenic tracer in the deep ACC upstream of Drake Passage, and subsequent measurements of tracer concentration throughout the southeastern Pacific and the Scotia Sea over the following years, to investigate the impact of turbulent mixing. The measured tracer distribution was used to infer turbulent diapycnal diffusivities (Watson et al., 2013; Zika et al., 2020), along with independent microstructure measurements of diffusivity (L. St. Laurent et al., 2012; Sheen et al., 2013; Merrifield et al., 2016), which are compared to our model diffusivity in figure 1c. Mashayek, Ferrari, et al. (2017) showed that their version of this model reproduced the spreading of the DIMES tracer using an imposed diapycnal diffusivity distribution based on observations. The current version of the model has increased vertical resolution, allowing a better representation of topographically generated processes such as lee waves, and an improved sponge layer to reduce spurious processes at the open boundaries. We also use an online parameterization of diapycnal diffusivity (to be discussed later) rather than a static 'map', in order to represent the mixing associated with instability of resolved small-scale processes.

The simulation starts in July 2009 (corresponding to the period following the DIMES tracer release), and is integrated for 100 days. We use the final 30 days of the simulation

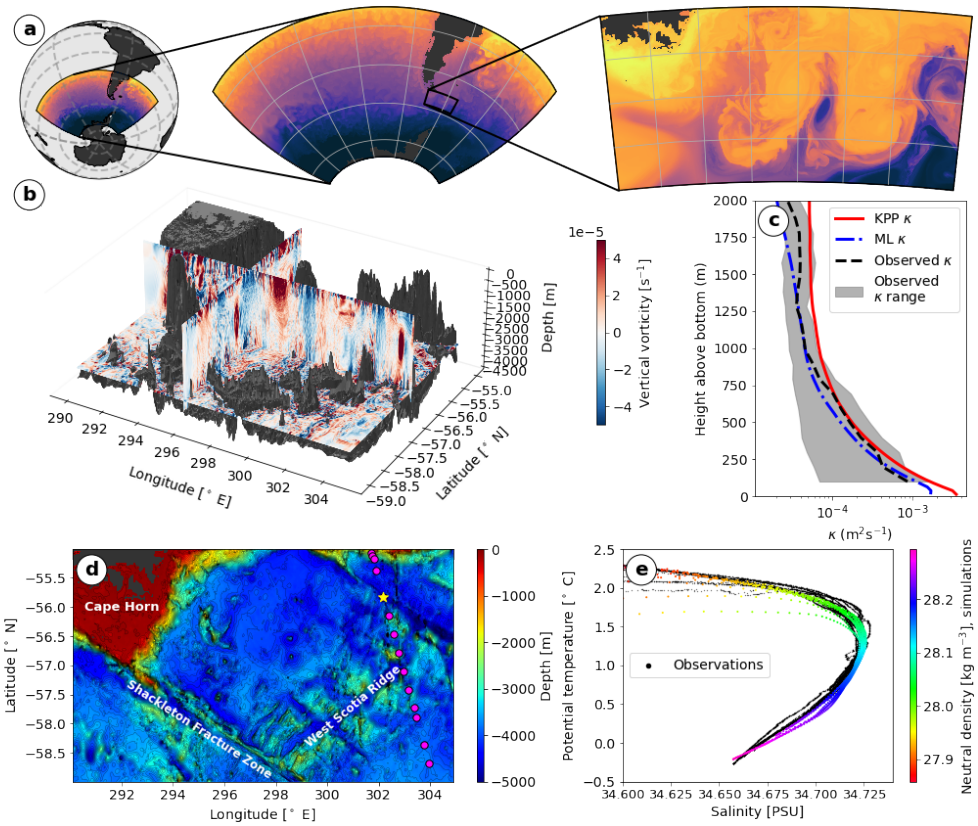

Figure 1. (a) Nesting diagram for Drake Passage model, showing parent simulation domain (left) and the Drake Passage domain presented here (right). (b) A daily average of vertical vorticity in the model. (c) Comparison of parameterized KPP diffusivity averaged with reference to height above bottom over the domain with microstructure observations from the Drake Passage (Merrifield et al., 2016) and a machine learning estimate of diffusivity (see §7). (d) Map of the simulation domain; shading and contours show depth. SR1b section stations are shown in pink, and the yellow star indicates the station at which profiles in figure 4 are taken. (e) Temperature-salinity diagram for the SR1b section observations and simulation data shown in figure 2. Simulation data are shaded with neutral density.

(early September to early October) for our analyses, with numbering of days referring to days from the start of this selected period.

The model is nested within a simulation of a larger region of the Southern Ocean, described in Tulloch et al. (2014) and shown in figure 1a. The larger simulation is itself forced at the open boundaries by restoring velocity, temperature and salinity to the Ocean Comprehensive Atlas (OCCA), a 3-year-long ocean state estimate that assimilated altimeter data, satellite sea surface temperature, and Argo profiles (Forget, 2010). The hydrography and eddy kinetic energy of the larger simulation was verified against observations by Tulloch et al. (2014). Neither this simulation, nor ours, includes tidal forcing, thus the interaction of tides with topography and corresponding generation of internal tides is not represented in our model.

Our nested simulation uses open boundary conditions derived from the parent simulation for sea surface height, potential temperature, salinity, and meridional and zonal velocities. In addition, a restoring boundary condition creates a sponge layer of 1 degree thickness (removed for analysis purposes, except in figure 3) in which the potential temperature, salinity, and zonal and meridional velocities are relaxed to the parent simulation. The model hydrography is therefore expected to be realistic, and can be compared to in-situ observations.

To validate the salinity, potential temperature, and neutral density in our simulation, we use a set of shipboard conductivity-temperature-depth (CTD) observations that were performed as part of the ACCLAIM (Antarctic Circumpolar Current Levels by Altimetry and Island Measurements) project along the SR1b section in the Drake Passage in November 2009. The stations at which observations were taken are shown in figure 1d. We sample our simulation at these locations for a like-for-like comparison, and in both cases compare potential temperature, practical salinity, and neutral density (Jackett & Mcdougall, 1997). The date of the fields sampled in our simulation is 10^{th} October 2009 (day 30), which is close to the observations in November 2009.

Figure 2 shows the observational data (left) and simulation data (right). Although expectedly not identical (see later discussion of temporal variation of deep-ocean water masses), there is very good agreement in temperature, salinity, and neutral density. In both cases, a bottom layer of fresh, cold, dense water underlies saltier, warmer, lighter waters. A temperature-salinity diagram (figure 1e) for the observations (black) and simulation (colour) at the locations in figure 2 confirms the agreement between observations and simulation.

Turbulent processes and their associated mixing are not explicitly resolved in the model, and must be parameterized. Typically, transition to turbulence occurs due to increased vertical shear (shear instability), or unstable buoyancy gradients (convective instability), although other instability mechanisms such as symmetric and inertial instabilities can also be the primary cause of instability in geophysical flows, leading to secondary shear or convective instabilities (Thomas et al., 2013; A. C. Naveira Garabato et al., 2019). The susceptibility of flows to be unstable to shear and convective instabilities can be captured by the Richardson number $Ri = N^2/S^2$, which quantifies the ratio of the stabilising effect of stratification N^2 to the destabilising squared vertical shear of horizontal velocities S^2. The stratification $N^2 = \partial b/\partial z$ is defined to be the vertical gradient of buoyancy $b = -\rho g/\rho_0$, where ρ is the density and ρ_0 is a reference density, and the squared shear is given by $S^2 = (\partial u/\partial z)^2 + (\partial v/\partial z)^2$, where u and v are the zonal and meridional velocities respectively.

Stratified shear instability can be shown analytically to be possible below a critical Richardson number $Ri_c = 0.25$ by the Miles-Howard Theorem (Miles, 1961; Howard, 1961), although at finite model resolution it is not clear what Ri_c should be, and several shear instabilities can occur for $Ri \sim O(1)$ (Caulfield, 2021). Convective instability occurs when $Ri < 0$, corresponding to unstable vertical buoyancy gradients with $N^2 < 0$. Susceptibility to submesoscale instabilities, such as symmetric and inertial instabilities, can also be quan-

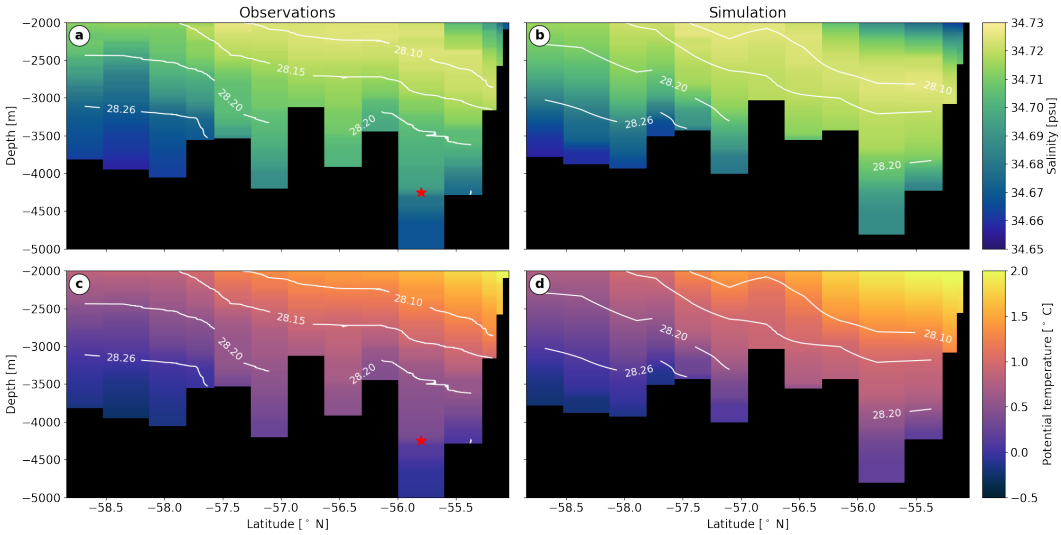

Figure 2. Comparison of (top) salinity and (bottom) potential temperature between (right) simulation and (left) observations. Contours indicate neutral density. Observations are from the SR1b section, collected in November 2009 as part of cruise JR195 of the ACCLAIM project, with locations shown in figure 1d. Simulation data are from a daily average on day 30, corresponding to 10^{th} October 2009, and sampled at the same locations as the observations.

tified using a Richardson number criterion, which reduces to $Ri < 1$ for larger-scale flows in which the Earth's rotation dominates inertial forces (Thomas et al., 2013). Support for a criticality condition in Ri being appropriate in an oceanic context is given by evidence for 'marginal instability'; that is, observations of the Richardson number in an oceanic flow fluctuating close to some critical value, typically near 0.25 (Thorpe & Liu, 2009; Smyth, 2020; Mashayek, Baker, et al., 2022).

The essence of Ri criticality is captured by the K-profile parameterization (KPP) (Large et al., 1994), which enhances the vertical diffusivity κ when $Ri < Ri_c$. Here, we use the KPP parameterization with $Ri_c = 1/3$, which is a reasonable measure of turbulence stability in an environment when some background turbulence exists; see Mashayek et al. (2021); Mashayek, Baker, et al. (2022) for a discussion. In order to validate the use of this parameterization, we compare diffusivity averaged in height-above-bottom coordinates throughout our domain with DIMES observational, microstructure-based estimates of diffusivity in the Drake Passage obtained by Merrifield et al. (2016). Figure 1c shows these profiles, which, subject to observational uncertainty, assumptions with respect to mixing efficiency (Osborn, 1980; Gregg et al., 2018), and the known temporal and spatial variability of mixing events (Moum, 2021), confirm that KPP does a satisfactory job in this domain, at least when averaged with reference to height above bottom.

We parameterize mixing in this way to support our goal of demonstrating the processes that lead to the transformation of AABW. However, in §7, we discuss the sensitivity of water mass transformation to the parameterization of mixing, by presenting an independent, offline machine learning estimate of diffusivity in our domain. This will highlight the need for more sophisticated parameterization of oceanic processes at the sub-grid-scale of ocean models.

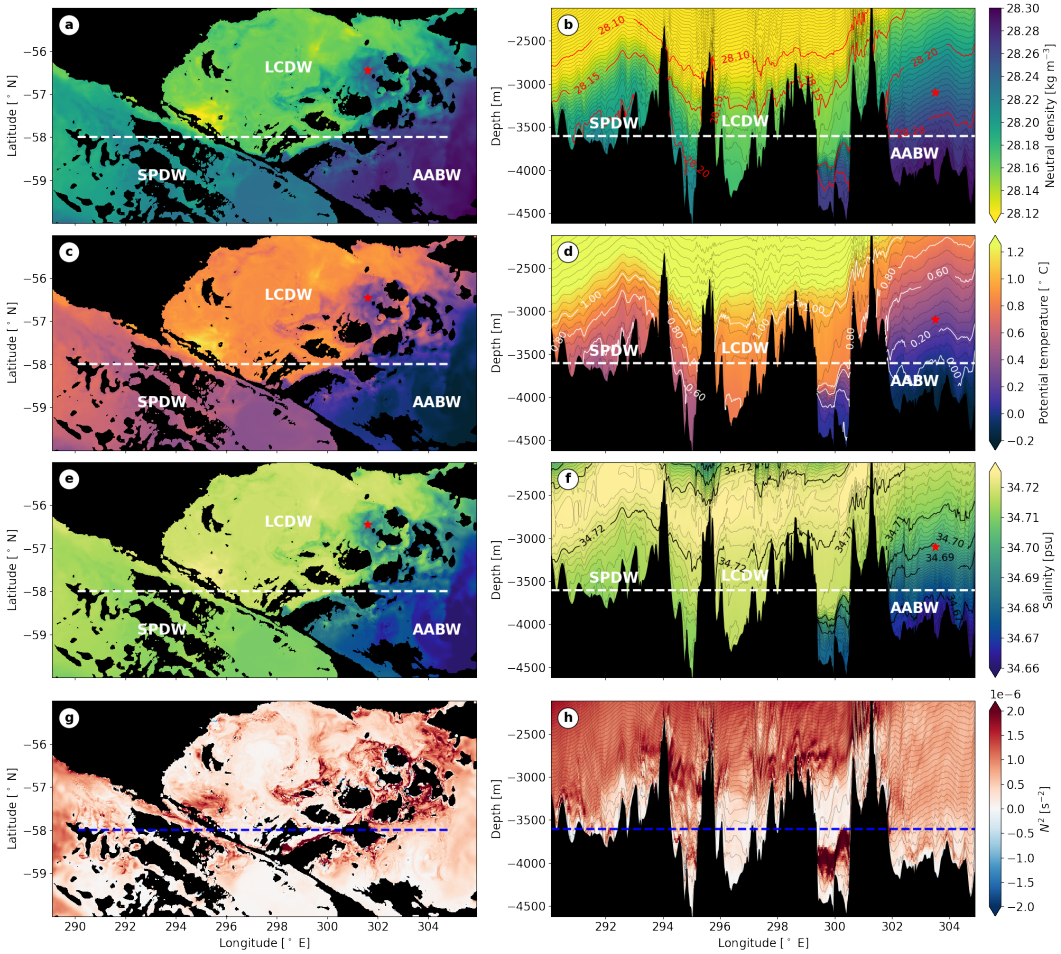

Figure 3. (a,b) Neutral density, (c,d) potential temperature, (e,f) salinity, and (g,h) stratification N^2 at (left column) 3600 m depth and (right column) -58° N. White and blue dashed lines show correspondence between columns. Red stars indicate locations of mixed AABW/SPDW referred to in the main text. A corresponding movie is available in the supporting information (movie S1).

3 Water mass classification

The Southern Ocean connects the major ocean basins (with the exception of the Arctic), and is a hub for global deep water masses. The lack of continental boundaries at the latitude band of the Drake Passage allows the strong westerly winds to draw deep isopycnals up to the surface, along which the deep waters of the global ocean can upwell and ventilate at the surface (Toggweiler, 1994; Lumpkin & Speer, 2007). The Drake Passage region is home to several distinct water masses formed in different parts of the global ocean. These water masses can be identified by their temperature, salinity and density properties, as well as by tracers such as oxygen, silicate and others (Tomczak & Large, 1989; Purkey et al., 2018; Liu & Tanhua, 2021). Here, we focus on temperature, salinity and neutral density, as tracers that can be calculated from our model.

The primary water mass of the Drake Passage, and of the Southern Ocean, is Circumpolar Deep Water (CDW), which is advected around the Southern Ocean by the ACC. The denser class of this CDW is called Lower Circumpolar Deep Water (LCDW), and occupies the neutral density range between 28.0 kg m^{-3} and 28.26 kg m^{-3} (NG02a). LCDW is

characterised by a salinity maximum that is derived from North Atlantic Deep Water in the Atlantic sector (Sievers & Nowlin, 1984, NG02a). A. C. Naveira Garabato, McDonagh, et al. (2002) (hereafter, NG02b) define LCDW in the Drake Passage as having salinity generally above 34.70, exceeding 34.73 at its mid-depth maximum, and potential temperature between 0.2 and 1.9° C. An additional dense variety of LCDW in the Drake Passage resulting from interaction of LCDW with the deep waters of the Ross Sea was defined by Sievers and Nowlin (1984). This Southeast Pacific Deep Water (SPDW) is characterised by neutral densities between 28.2 and 28.26 kg m^{-3}, and is colder than 0.6 °, and fresher than 34.71 (NG02a).

AABW is defined by NG02a to have neutral densities greater than 28.26 kg m^{-3}. In the Drake Passage, the relevant variety of AABW is Weddell Sea Deep Water (WSDW), which is formed in the Weddell Sea to the south of the Drake Passage by the mixing of dense, shelf-derived Weddell Sea Bottom Waters with CDW. WSDW flows northward at depth over the South Scotia Ridge and into the Scotia Sea before reaching the Drake Passage (NG02b). Using a global simulation with a tracer injection in the Weddell Sea, Solodoch et al. (2022) showed that WSDW travels only downstream of the Drake Passage, with high concentrations in the Atlantic basin, and eventually occupying the Indian basin and west Pacific basin. WSDW is fresher, colder and denser than the overlying LCDW.

Figures 3a,c,e show neutral density, potential temperature, and salinity at 3600 m depth in the simulation. At this depth, there is a clear demarcation of three distinct water masses, separated from each other by the north-west/south-east running ridge of the Shackleton Fracture Zone, and the south-west/north-east running West Scotia Ridge system (see figure 1d for labelling of bathymetric features). The vertical structures of these water masses are illustrated in figures 3b,d,f, with the dashed lines showing the depth and latitudinal correspondence between the left and right columns. Movie S1 shows some of these panels over a 30-day period, and reveals that the locations and depths of the water masses vary with time.

With reference to the above definitions of Drake Passage water masses, figure 3b shows that most of the domain below 2000 m depth is filled with LCDW. The salinity maximum described above that is characteristic of LCDW is evident in figure 3f, and has a value of 34.73. The denser, fresher waters of the LCDW below 28.2 kg m^{-3} can be identified as SPDW. At 3600 m depth, there is a clear lateral boundary (seen in figures 3a,c,e) between the denser SPDW and the lighter class of LCDW, formed by the ridge of the Shackleton Fracture Zone. The denser SPDW is unable to overflow this ridge, so the basin in the north of the domain is filled with the lighter LCDW only, as can be seen in figures 3b,d,f.

The neutral density contour of 28.26 kg m^{-3}, potential temperature contour of 0.2°C, and salinity contour 34.69 are almost co-located, consistent with the definition by NG02b, of the boundary between LCDW and the colder, fresher WSDW. WSDW is only present in the south-east of the domain, consistent with its origin in the Weddell Sea and westward path from the South Scotia Ridge to the Drake Passage. From figure 3a,c,f, it is clear that WSDW is also topographically bounded - to the west from the SPDW by the Shackleton Fracture Zone, and to the north-west by the West Scotia Ridge. Some lighter WSDW does however overflow the West Scotia Ridge, in particular during a significant event around day 20 (visible in movie S1, and to be discussed further in §5.3.2). This highlights the temporal variability of the water mass locations.

4 Stratified water mass interfaces

There are often sharp interfaces between the different water masses in the simulation, with corresponding high stratification due to their differing densities. Figures 3g,h show that stratification is enhanced at several interfaces in the domain. The elevated stratification is due to sharp gradients in both salinity (figure 3b) and temperature (figure 3d). This is

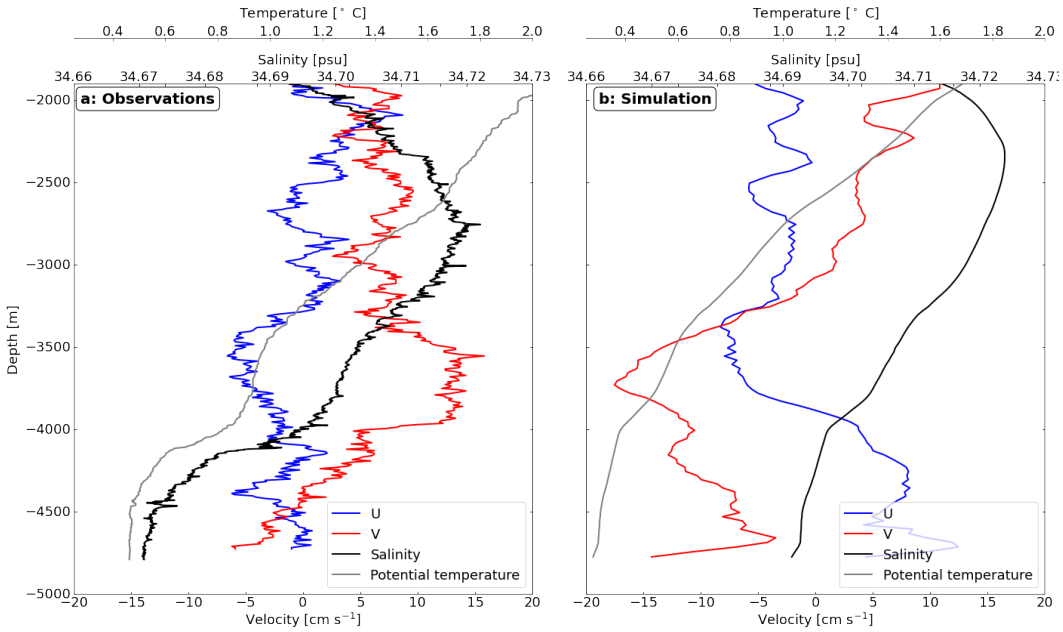

Figure 4. Velocity, temperature and salinity profiles at the location shown by the yellow star in figure 1d. Steps in temperature and salinity are accompanied by strong vertical shear of horizontal velocities. (a) In-situ observational data from DIMES, March 2013; and (b) simulation data on day 0.

consistent with the observations of Sievers and Nowlin (1984), who, on investigating the various water masses of the Drake Passage, found that they were generally separated by highly stratified interfaces, which they termed stability strata.

Steps in salinity and temperature have been previously observed at many locations in the global ocean, and interpreted as boundaries between water masses; in particular in the Drake Passage (Sievers & Nowlin, 1984), the East Scotia Sea (Meredith et al., 2013), and the South West Atlantic (Reid et al., 1977). In the observations shown in figure 2a,c, sharp gradients in temperature and salinity are also visible, for example at the location marked by a red star.

In a different set of observations along transect SR1b, taken by the DIMES project in March 2013, there are similar steps in temperature and salinity at depth, which were co-located with high vertical shear as measured with a lowered acoustic Doppler current profiler (ADCP). These steps and the corresponding velocities are shown in figure 4a, with one such step and associated sharp vertical velocity gradient located just below 4000 m depth. A corresponding profile at the same location from the simulation is shown in figure 4b, also demonstrating a step in temperature and salinity just above 4000 m depth, with co-located vertical gradients in horizontal velocities. The occurrence of vertical shear of horizontal velocities at a sharp density interface might be expected if the interface is tilted horizontally, creating a strong horizontal buoyancy gradient and thereby vertical shear, in order to maintain thermal wind balance. We will later demonstrate this mechanism using the simulation.

The presence of sharp interfaces between water masses and the corresponding high stratification, both in observations and in our model, is of great interest, as it is likely to relate to how AABW mixes with overlying waters. Can the sharpness of an interface give

us insight into the mixing that its bounding water masses have experienced in the past, or are there other mechanisms that generate and destroy strong interfacial gradients?

There is evidence in the simulation (for example, at locations marked with a red star in figure 3) of waters that have properties intermediate between those of WSDW and LCDW. These waters are lighter than 28.26 kg m^{-3} (i.e. lighter than WSDW), but are also fresher than the freshest LCDW (SPDW) entering from the west of the domain. Thus, the waters in question are likely to be the result of WSDW mixing with the LCDW above. NG02a note that the WSDW entering the Drake Passage from the east is the lightest fraction of WSDW overflowing the South Scotia Ridge from the Weddell Sea, and is warmer and more saline than 'pure' WSDW following intense diapycnal mixing with LCDW (specifically, SPDW) on its westward transit to the Drake Passage. The easternmost part of the domain shown in figure 3b,d,f,h does not exhibit a sharp interface between AABW and SPDW, suggesting that the water masses have been rather thoroughly mixed.

However, elsewhere in the domain, strongly stratified interfaces do exist, albeit not always exactly aligned with the definitions given above for the LCDW/SPDW/WSDW boundaries (e.g., see figure 3h). These interfaces are also present in the larger SO simulation in which this model is nested (see §2 and figure 1a), which can resolve them with its vertical resolution of 50 m. The interfaces may therefore be inherited from observations via this larger model and the ocean state estimate with which it is itself forced. Although it is possible that the sharp interfaces are purely inherited remnants of the initial meeting of the distinct water masses (and a lack of mixing between such waters), the spatial heterogeneity of interface sharpness points to the leading-order involvement of a dynamical mechanism besides mixing. In the upper ocean, frontogenesis is well known to sharpen pre-existing horizontal density gradients (Hoskins, 1982; McWilliams, 2021), and there is also evidence of frontogenesis acting at submesoscale fronts in the ocean interior (Siegelman et al., 2020). It is clear from figure 3h that interfaces are often tilted from the horizontal. This is likely due to the flow moving over large-scale bottom topography, geographical variations in the water mass locations, and the passing of mesoscale eddies. The horizontal tilting of interface results in horizontal density gradients; frontal processes may therefore occur in the deep ocean to sharpen or widen these ambient gradients.

A further implication of the occurrence of water mass interfaces is the modification of dynamics associated with the layer of high stratification itself. Next, we investigate the potential impact of water mass interfaces on mixing processes in the deep ocean.

5 The phenomenology of topographic mixing

We wish to understand how different physical processes contribute to enhancing turbulence near topography. As discussed in §2, the Richardson number $Ri = N^2/S^2$ can be used to quantify the susceptibility of a flow to shear and convective instabilities, and it is a Richardson number-based criterion that informs the mixing parameterization in the model. We therefore consider mechanisms that decrease stratification N^2 and increase vertical shear S^2 as a proxy for enhancing diapycnal mixing on the sub-grid-scale.

5.1 The nature of modelled mixing

Figure 5 and the corresponding movie S2 illustrate the complex dynamics of flow-topography interaction in the simulation. Figure 5a shows the Richardson number, and figure 5b the corresponding vertical diffusivity κ, for an hourly average of a section of the simulation at -57° N. In general, κ is at its background value of 5 $\times 10^{-5}$ m^2 s^{-1} outside of the bottom few hundred metres, and outside of the upper-ocean mixed layer (not shown), corresponding to Richardson numbers greater than the critical value $Ri_c = 1/3$ used here. In some locations, breaking topographic waves enhance κ up to 1000 m above the bottom. Within the bottom few hundred metres, κ is enhanced by the KPP

parameterization due to shear instability ($0 < Ri < Ri_c$) or convective instability ($Ri < 0$). From consideration of the stratification (figure 5c) and squared vertical shear (figure 5d), it is clear that many of the areas of enhanced κ are due to both high shear and low stratification, acting together to decrease Ri. Furthermore, figure 5c shows that there are several areas of unstable stratification close to the boundary, indicating conditions for convective instability and overturning. These patches of $N^2 < 0$ are a feature throughout the domain, and play an important role in the near-boundary dynamics.

To understand how these areas of convective instability form, we can consider the simple unforced buoyancy equation:

$$\frac{\partial b}{\partial t} = -\mathbf{u} \cdot \nabla b + \frac{\partial}{\partial z}\left(\kappa \frac{\partial b}{\partial z}\right) \ , \tag{1}$$

where b is buoyancy, $\mathbf{u}$ is velocity, and the horizontal component of diffusion is taken to be zero, since the vertical gradients of the density and turbulent density flux tend to dominate over the horizontal components (Ferrari et al., 2016). Taking the vertical derivative, we obtain:

$$\frac{DN^2}{Dt} = \underbrace{-\frac{\partial \mathbf{u}_H}{\partial z} \cdot \nabla_H b}_{\text{(A)}} \underbrace{- \frac{\partial w}{\partial z} N^2}_{\text{(B)}} + \underbrace{\frac{\partial^2}{\partial z^2}\left(\kappa N^2\right)}_{\text{(C)}} \ , \tag{2}$$

where $D/Dt \equiv \partial/\partial t + \mathbf{u} \cdot \nabla$ is the full derivative following a water parcel, and H represents the horizontal components of velocity and the gradient operator.

Each of the three terms on the right hand side of equation (2) represents a way in which the stratification following a water parcel can change. Term (C) encapsulates vertical diffusion, and it is through this term that turbulent processes (represented within the parameterized turbulent diffusivity κ) act to diffuse vertical gradients in buoyancy, thereby causing irreversible mixing. The vertical gradients of κ and N^2 and corresponding turbulent buoyancy fluxes play a leading-order role in the boundary layer dynamics (Polzin & McDougall, 2022). However, this term alone cannot change the sign of N^2 from positive to negative. Suppose that (A) and (B) are zero, and that initially $N^2 > 0$ everywhere except on the boundary, and zero at the boundary itself since there should be no buoyancy flux across the boundary (an insulating boundary condition). Then, suppose that at some interior location N^2 becomes zero. Given $\kappa \geq 0$, this point is thus a local minimum of κN^2, so (C) is greater than zero, and $DN^2/Dt \geq 0$ by equation (2), hence the sign of N^2 cannot change.

Similarly, term (B), which represents changes to the vertical buoyancy gradient due to vertical convergence or divergence of the vertical velocity, cannot alone change the sign of N^2. If (A) and (C) are zero, the solutions to equation (2) are exponential, and thus single-signed.

Therefore, term (A) must be responsible for generating areas of convective instability from a stable flow. This term corresponds to vertical shear of horizontal velocities acting upon horizontal buoyancy gradients, which physical intuition confirms can overturn isopycnals – by advecting dense water above light water and creating conditions for convective instability.

An important aspect of term (A) is that, if the velocities and buoyancy gradients are in thermal wind balance, such that $\mathbf{f} \times \partial \mathbf{u}_H / \partial z = -\nabla_H b$, where $\mathbf{f} = (0, 0, f)$ with f as the Coriolis parameter, then (A) vanishes and this shear mechanism cannot cause overturning. Thus, for convective instability conditions to occur in the absence of forcing (such as surface cooling or bottom thermal flux), the flow must be unbalanced; this imbalance could be associated with internal gravity waves, fronts, or boundary processes.

The preceding analysis serves to highlight the important role of vertical shear in generating conditions for instability. Not only is vertical shear needed to destabilise a statically

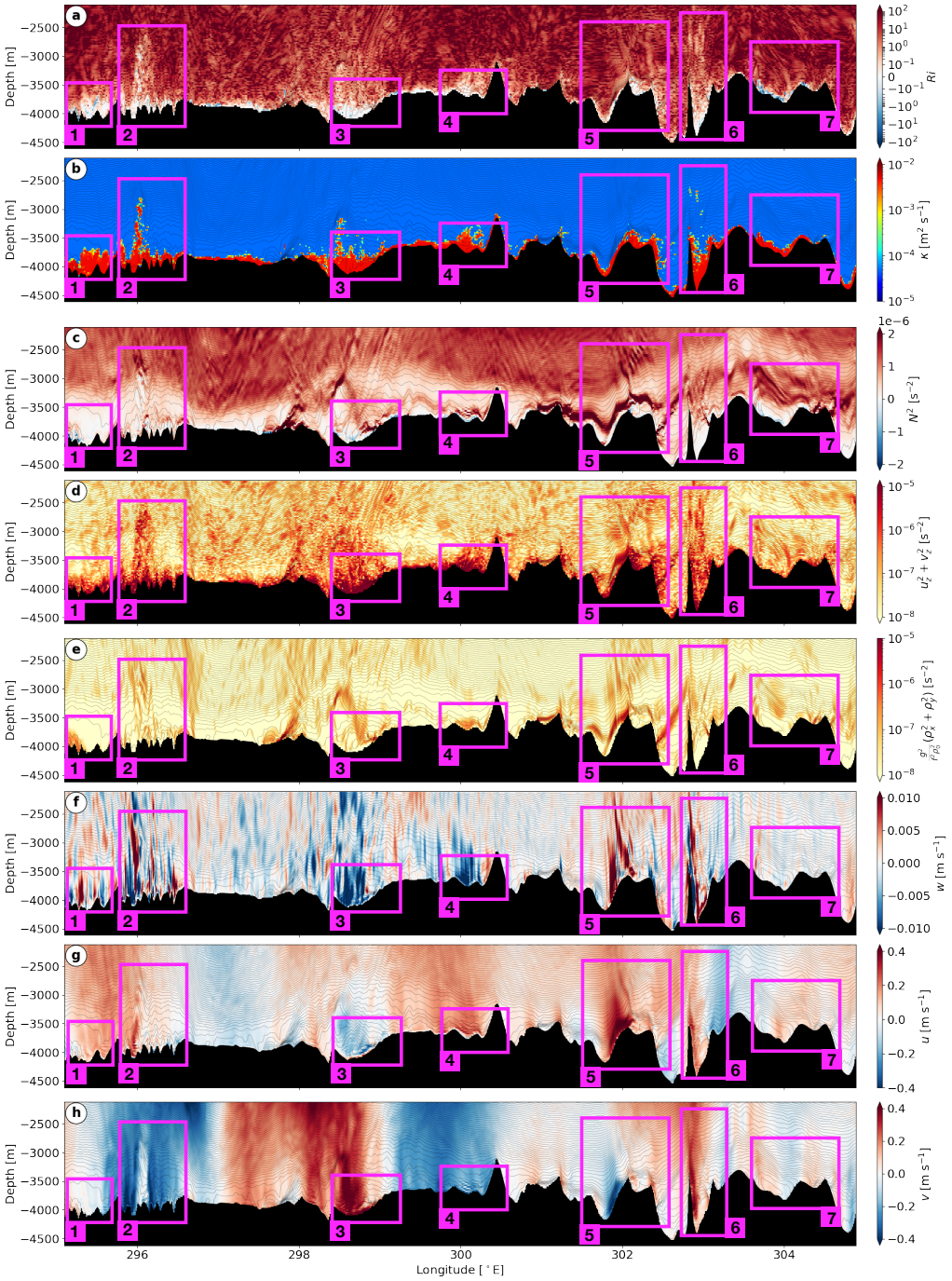

Figure 5. Various dynamical variables at -57 ° N, demonstrating a range of mixing processes. (a) Richardson number, (b) vertical diffusivity, (c) stratification, (d) squared vertical shear of horizontal velocities, (e) squared vertical shear of horizontal velocities, as implied by the thermal wind balance relation applied to the horizontal density gradients, (f) vertical velocity, (g) zonal velocity, and (h) meridional velocity. Magenta boxes highlight processes discussed in the main text. A corresponding movie is available in the supporting information (movie S2).

stable flow via the onset of shear instability, but it is also required to create the conditions for convective instability from horizontal buoyancy gradients. Having identified the role of vertical shear in creating the conditions for mixing, we now discuss the physical processes that govern vertical shear near the boundary.

5.2 Topographically-induced processes

First, we consider the complex topographic interaction processes that take place in the absence of the highly stratified interfaces separating the different water masses. Then, we examine the processes arising from the these interfaces' presence.

5.2.1 Boundary layer frictional processes

Wherever a flow encounters a boundary with friction (see Appendix A for a description of the modelled no-slip boundary condition), shear may arise as the flow experiences drag in a thin boundary layer. This drag alone can be expected to create shear even when the topography is flat, and it is clear from figure 5d that vertical shear is always enhanced near the boundary.

In a rotating geophysical flow, the force balance between friction, rotation, and pressure gradients modifies the boundary layer dynamics by generating an Ekman spiral, in which the flow turns clockwise (in the Southern Hemisphere) as the boundary is approached. We find that the flow direction, averaged over the entire simulation domain, turns on average 12° clockwise in the bottom 25 m, and on average 4° clockwise in the 25 m above this, consistent with Ekman theory. We are therefore permitting Ekman dynamics at the bottom boundary, but not fully resolving them, since the depth of the Ekman layer is of the same order as the 25 m vertical grid resolution.

When the bottom boundary is sloped, these dynamics become more complex yet. A cross-slope flow can induce an upslope or downslope Ekman current, which can become arrested by the restoring buoyancy force on isopycnals (MacCready & Rhines, 1991; Garrett et al., 1993; Ruan et al., 2019, 2021). An example of a near-boundary flow that is consistent with an unsteady upslope Ekman current is shown by the zonal and meridional velocities in figure 5g,h in box 3, in which the flow turns clockwise in the bottom few grid cells, with the corresponding enhanced vertical shear shown in figure 5d. Observational evidence suggests that a downslope Ekman flow can generate low stratification and large shear near topography, producing conditions favourable for the development of submesoscale instabilities and intense mixing in a deep western boundary current (A. C. Naveira Garabato et al., 2019; Spingys et al., 2021). Numerical studies also suggest that submesoscale instabilities during Ekman adjustment may have an overlooked role in topographic mixing (Callies, 2018; Wenegrat & Thomas, 2020). However, the rough topography and unsteady, energetic nature of the flow in the Drake Passage suggests other explanations for the elevated diffusivities several hundred metres above topography seen in this model.

5.2.2 Lee waves, blocking, and breaking

When stratified flows interact with rough topography, a number of processes can occur that generate turbulence and mixing. For topographic wavenumbers $\mathbf{k}$ such that $f^2 < (\mathbf{U} \cdot \mathbf{k})^2 < N^2$, where $\mathbf{U}$ and N are the near-bottom velocity and stratification, vertically propagating lee waves are generated. Lee waves extract energy from the mean flow and cause turbulent mixing when they break. They are thought to be a leading-order source of mixing in the Southern Ocean (A. Naveira Garabato et al., 2004; Scott et al., 2011; Nikurashin & Ferrari, 2011; Trossman et al., 2013; De Lavergne et al., 2016).

A recent study of the lee wave field in this simulation found that there was strong and nonlinear lee wave generation throughout the domain, especially in areas of rough

topographic features such as the Shackleton Fracture Zone and the West Scotia Ridge, and in areas of high bottom currents (Baker & Mashayek, 2022). The vertical velocity, shown in figure 5f, exhibits (for example, box 2) lee waves generated at topography and propagating vertically upwards. In this simulation, lee waves can propagate through the entire water column and interact with the surface (Baker & Mashayek, 2021).

The mechanisms of lee wave breaking and resulting vertical distribution of mixing are poorly constrained (Legg, 2021). In the presence of a strong lee wave field in the simulation, there is enhanced diffusivity in the bottom 100-400 m (e.g., boxes 1 and 2, figure 5b), consistent with the results of Klymak (2018) for idealised simulations with representative Southern Ocean parameters and multi-scale topography. The waves generate high shear and even areas of static instability in the lee of topography (figure 5c, box 2), and thus contribute significantly to mixing near topography.

Above the bottom few hundred metres, the modelled lee waves generally do not become shear- or convectively unstable, so vertical diffusivity is not enhanced by the KPP parameterization and, instead, the waves experience the background diffusivity. However, in some locations, highly nonlinear lee waves do become unstable up to 1000 m above the bottom, such as in box 2 (figure 5b,f).

The lack of any significant interior lee wave-driven mixing in the simulation suggests a need for better parameterization of mixing driven by nonlinear wave interactions in the ocean interior in models such as this that resolve only part of the internal wave spectrum. However, the ultimate sink for lee wave energy in the interior remains poorly understood. Observations in the Drake Passage have shown that rates of dissipation are an order of magnitude smaller than would be expected if all lee wave energy was dissipated locally near topography, which suggests that the waves have an energy sink elsewhere (Sheen et al., 2013; Waterman et al., 2013, 2014; Cusack et al., 2017; Voet et al., 2020; Gutierrez-Villanueva et al., 2022).

The topographic Froude number $Fr = Nh/|\mathbf{U}|$, where h is the characteristic height of topography, indicates the nonlinearity of the generated lee wave field. When $Fr \gtrsim 1$, the flow cannot all go over a topographic obstacle, and is instead blocked or split, giving rise to non-propagating processes as well as a nonlinear propagating lee wave field. These non-propagating processes are also an important source of turbulence and mixing (Klymak, 2018; Klymak et al., 2021). Such processes include downslope windstorms (Klemp & Lilly, 1975; Peltier & Clark, 1979; Durran, 1986), hydraulic control and jumps (Winters & Armi, 2012, 2014), and wake vortices (Srinivasan et al., 2019), which can all generate high shear, instabilities, and mixing. Box 6 in figure 5 shows an example of flow interacting with a tall topographic feature. At its peak, lee waves are generated (visible in the vertical velocity field, figure 5f, box 6), but velocities are accelerated down to the feature's base as the flow is topographically steered (figures 5g,h, box 6). This generates shear (figure 5d, box 6) and high diffusivity (figure 5b, box 6).

5.3 Role of stratified interfaces

The layers of high stratification that separate the various water masses discussed in §3 can dynamically influence the topographic interaction processes discussed above, as well as creating new mechanisms of mixing.

5.3.1 Generation of vertical shear

The interfaces between different water masses can be identified by the layers of high stratification in figure 5c and movie S2, panel c. There is not one continuous interface, rather several interfaces, separating different layers of fluid that move throughout the domain (as illustrated by the salinity in movie S2, panel e). The complex patterns of the areas of high stratification in figures 3g,h are further evidence of this. The layers are not horizontal,

but undulate with the topography (e.g., figure 5c, box 5), with the geographical location of the water masses (e.g., figure 3b), and with the translation of mesoscale eddies through the domain. The tilting of these vertically stratified interfaces creates strong horizontal buoyancy gradients. In a non-rotating flow, baroclinic production of vorticity would act to flatten the tilted isopycnals. However, in a rotating fluid, geostrophic adjustment acts to increase vertical shear, such that the horizontal buoyancy gradients approach thermal wind balance.

Figure 5e shows scaled horizontal buoyancy gradient $g^2(\gamma_x^2 + \gamma_y^2)/f^2/\rho_0^2$, where g is the acceleration due to gravity, ρ_0 is a reference density, γ is the neutral density, and subscripts denote derivatives. Not only does this figure show that strong horizontal buoyancy gradients correspond to the stratified interfaces (e.g. box 5), but it can also be compared to the vertical shear in figure 5d. Were the flow in exact thermal wind balance, the two panels d and e would be identical. There is a clear correspondence between areas of high vertical shear (panel d), high horizontal buoyancy gradients (panel e), and stratified interfaces (panel c). The zonal and meridional velocities (panels g and h) also exhibit jets next to topography in box 5 due to the locally elevated vertical shear. Observational evidence for vertical shear associated with stratified interfaces was presented in figure 4a, and based on this and our simulation, we conclude that one of the mechanisms of generating vertical shear in the deep ocean is the tilting of water mass interfaces.

However, it is not clear that this vertical shear and the interfaces themselves can then cause instability. It was already shown in equation (2) that vertical shear in thermal wind balance cannot cause overturning, and the interfaces by definition possess large stratification N^2 alongside high squared vertical shear S^2; thus, the Richardson number is not necessarily reduced at the interfaces. For example, the regions of high shear in figure 5d, box 5, do not correspond to increased diffusivity in figure 5b. Instead, it is the interaction of the interfaces with topography that causes instability and generates mixing.

5.3.2 Interaction with topography

When the strong horizontal buoyancy gradients of the water mass interfaces interact with the rough topography of the Drake Passage, they frequently cause overturning of isopycnals and conditions for instability. Areas of unstable stratification near topography associated with the passing of horizontal gradients in buoyancy (tilted isopycnals) can be seen in figure 5c, boxes 1, 3, 4, and 7, and in movie S2. Friction at the boundary (§5.2.1) or small-scale topographic processes such as lee waves (§5.2.2) perturb and sometimes overturn tilted isopycnals as a dense water mass moves along topography, leaving behind it weakly stratified or unstable fluid. This mechanism relies strongly on the temporal variability of the water masses.

To demonstrate this temporal variability, we show in figure 6 and movie S3 an example of a fast-moving overflow of dense waters over the West Scotia Ridge. As discussed in §3, this class of water is lighter than the WSDW to the south-east of the domain, as it has mixed with LCDW above. The top row of figure 6 shows salinity at 3600 m depth, demonstrating how over a period of seven days, dense, fresh waters that were previously trapped by the ridge (e.g., see figure 3c, showing the salinity field on day 0) push through the topography and enter the northern part of the domain. This overflowing event is driven by fast northward velocities associated with a surface-enhanced mesoscale eddy that spans the entire water column (figure 6j,k,l). The corresponding motion of the stratified interface over topography contributes to turbulence and mixing in its wake.

The second row of figure 6 corresponds to the white dashed lines in the top row, and shows the progression of the denser water class as it flows northwards, using salinity as a tracer. There are several stratified interfaces, the movement of which is clear from the stratification time series in the third row, and from movie S3. Behind (to the south of) the contact point of the interfaces with topography, there are areas of negative stratification

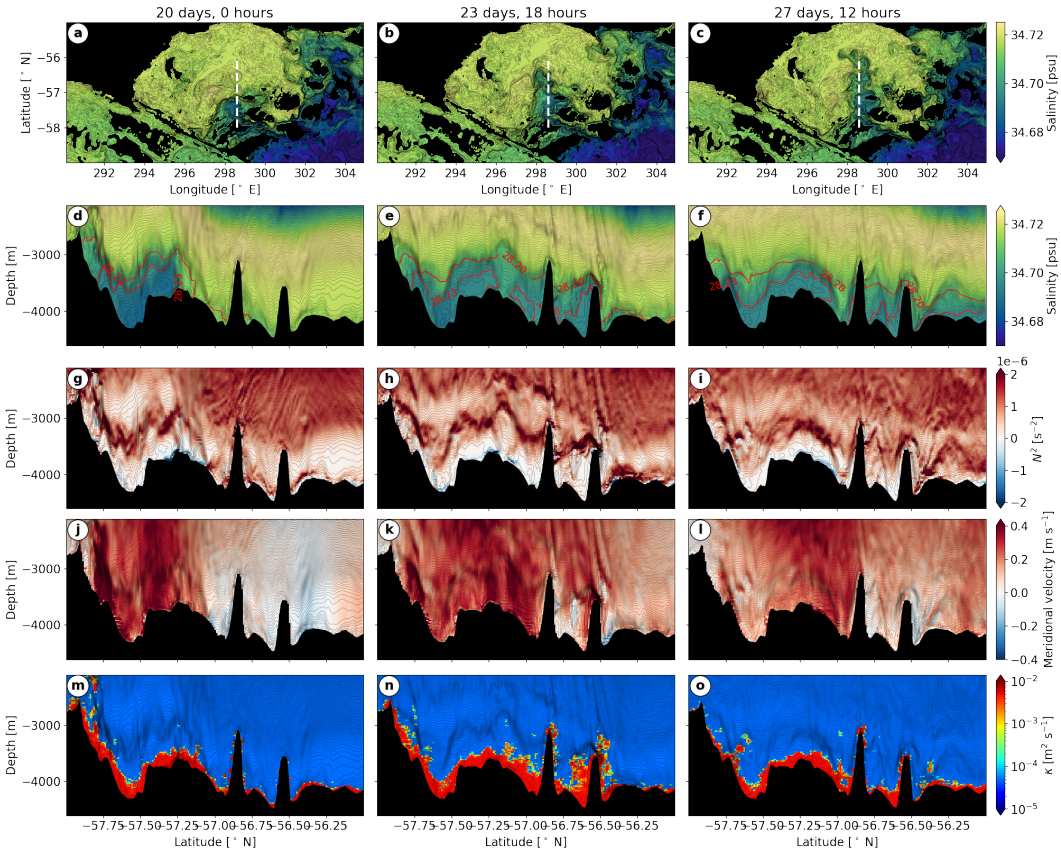

Figure 6. Time series (time increasing from left to right) over ∼ 7 days of an overflow of AABW passing northwards over the West Scotia Ridge. (a-c) Salinity at 3600 m depth, with white dashed line indicating the section shown in the remaining panels at 298.6° E. (d-f) Salinity, (g-i) stratification (or squared buoyancy frequency), (j-l) meridional velocity and (m-o) vertical diffusivity. All contours show neutral density. A corresponding movie is available in the supporting information (movie S3).

caused by the isopycnals overturning with the motion of the front. Beneath the interface, after the contact point has passed, the fluid is weakly stratified and the areas of negative stratification are persistent, slowly increasing in stability as they are mixed by the enhanced vertical diffusivity.

The fast flow speeds and tilted isopycnals of the dense bottom current moving over the rough topography result in increased diffusivity along the current's path, as shown in the bottom row of figure 6. We will later present evidence that this event is associated with increased upwelling of the dense waters.

5.3.3 Impact on propagating lee waves

The presence of the stratified interfaces near topography can also influence the generation, propagation and breaking of lee waves. While the deep ocean is generally considered to be weakly and uniformly stratified, the impact of a stratified interface has been extensively studied in the context of atmospheric mountain wave generation beneath a temperature inversion or the highly stratified stratosphere. The occurrence of hydraulic jumps, breaking lee waves, lee wave rotors (flow circulations in the lee of topography), resonant trapped lee waves on the interface, and downslope wind storms have been found to be highly dependent on the height of the stratified interface, the density difference across the interface, and the topographic Froude number Fr (Klemp & Lilly, 1975; Durran, 1986; Vosper, 2004; Sheridan & Vosper, 2006). Jagannathan et al. (2020) established that the location of a strong density step above topography impacted whether or not it plunged downwards in the lee of the topography, thereby giving rise to a wave field aloft that was six times more energetic than in the absence of interface plunging. Armi and Mayr (2015) found that when a strong density step exists above topography, this can act as a 'virtual topography' controlling the stratified flow response aloft. The presence of these density steps in the deep ocean could therefore have implications on the way we represent topography in oceanic lee wave parameterizations.

Away from topography, when encountering a region of high stratification, lee wave horizontal velocities increase, resulting in enhanced nonlinearity, wave overturning, and turbulence (Durran, 1986). Lee waves may also gain/lose energy to the mean flow or break at critical levels through interaction with the vertical shear associated with thermal wind balance of the tilted interfaces (Kunze & Lien, 2019; Baker & Mashayek, 2021). Abrupt changes to the the mean flow through which lee waves propagate, such as those linked to water mass interfaces, are largely neglected in the question of how and where lee waves dissipate their energy, but may be important for catalysing wave instability.

Evidence of impact of the layers of high stratification on lee waves can be seen in figure 5. In box 2, a lee wave breaking is evident in the diffusivity (figure 5b) up to the level where stratification increases significantly, suggesting that the enhancement in stratification may increase nonlinearity of the wave, causing it to lose energy by breaking. In box 5, a wave is generated above a strongly stratified interface, suggesting that the interface may be acting as a 'virtual topography' (Armi & Mayr, 2015). A large lee wave is also generated by the interaction of the front of the dense bottom current with topography in figure 6k at -56.5° N. It is clear that the presence of stratified interfaces in the Drake Passage may alter the nature of lee wave generation, propagation and breaking, potentially modifying the distribution of lee wave mixing in a way that would be difficult to take into account in parameterizations.

6 Water Mass Transformation

In order to understand how deep waters are transformed to different densities by diapycnal mixing, we calculate the water mass transformation rate, equivalent to the diapycnal velocity integrated over a density surface. In particular, it is key to elucidate whether waters

at some density level upwell (become lighter), or downwell (become denser). This question gives rise to a conundrum that has been the topic of active research over the past decade (De Lavergne et al., 2016; Ferrari et al., 2016). The diapycnal turbulent flux of buoyancy F_b can be approximated using a diffusive flux law, $F_b = -\kappa N^2$, where κ is the vertical diffusivity (Osborn, 1980). If $\frac{\partial F_b}{\partial z} < 0$, then waters become lighter (upwelling), whereas if $\frac{\partial F_b}{\partial z} > 0$, waters become denser (downwelling). Thus, if, as is generally observed, κ significantly increases towards topography without a corresponding decrease in N^2, then $\frac{\partial F_b}{\partial z} > 0$ and downwelling occurs rather than the necessary upwelling.

A resolution to this conundrum has been suggested by noting that at the bottom boundary, in the absence of geothermal heat flux, an insulating boundary condition implies that $F_b = 0$. Thus, in some boundary layer, F_b (which is strictly negative for stable vertical buoyancy gradients) must decrease with height above bottom, implying upwelling. This has given rise to an increasingly accepted theory that waters generally downwell in the stratified ocean interior, with this downwelling compensated by strong upwelling near topography – resulting in net upwelling (Ferrari et al., 2016; McDougall & Ferrari, 2017; Drake et al., 2020). Here, we are able to verify this theory within the context of our simulation, subject to model constraints on resolution of the bottom boundary layer and uncertainties in the parameterization of vertical diffusivity.

6.1 Water mass transformation framework

We first define the diapycnal velocity $\tilde{\mathbf{e}}$, that is the velocity in the cross-density surface direction. By subtracting the motion of an isopycnal surface itself from the Eulerian velocity of a water parcel, Ferrari et al. (2016) show that

$$\tilde{\mathbf{e}} = \frac{\nabla \cdot \mathbf{F_b}}{|N^2|}\mathbf{n} \ , \tag{3}$$

where $\mathbf{F_b}$ is the buoyancy flux, and $\mathbf{n}$ is the normal to the isopycnal surface defined as pointing towards higher buoyancy. Note that this may not always be in the positive vertical direction, and as such our definition of 'upwelling' refers to upwelling in buoyancy space, which may be vertically downwards in the presence of unstable stratification. We approximate the divergence of the buoyancy flux by $\nabla \cdot \mathbf{F_b} \sim -\partial(\kappa N^2)/\partial z$. This approximation is often made due to the occurrence of significantly larger vertical buoyancy gradients than horizontal ones in the ocean interior, and here we do not apply a horizontal diffusivity in the model, so do not have explicit horizontal buoyancy fluxes. The vertical buoyancy flux $F_b = -\kappa N^2$ is set to zero at topography to satisfy the insulating boundary condition.

In order to quantify upwelling over a density surface, we use the water mass transformation framework of Walin (1982); Ferrari et al. (2016). The diapycnal velocity integrated over a neutral density surface $A(\gamma)$ is denoted $\mathcal{E}(\gamma)$, where γ is neutral density, and is given by:

$$\mathcal{E}(\gamma) = \int_{A(\gamma)} \tilde{\mathbf{e}} \cdot \mathbf{n} \, dA \simeq -\frac{\rho_0}{g}\frac{\partial}{\partial \gamma^*}\int_{\gamma > \gamma^*} \frac{\partial}{\partial z}(\kappa N^2)\, dV \ . \tag{4}$$

6.2 Simulated water mass transformation

A 30-day average of the diapycnal velocity $\tilde{\mathbf{e}} \cdot \mathbf{n}$, with $\tilde{\mathbf{e}}$ as defined in equation (3), along -57° N, is shown in figure 7a. Notice (red) upwelling close to topography in the bottom 50-100 m, with (blue) downwelling just above, consistent with the concept of upwelling in a boundary layer, with downwelling in the stratified interior above. The upwelling occurs due to complex topographic interaction processes in the bottom boundary layer creating vertical gradients in stratification and diffusivity such that $\frac{\partial F_b}{\partial z} < 0$. In particular, areas of unstable stratification near the boundary can reverse the direction of the normal vector in equation (3), causing downwards diapycnal velocities that correspond to upwelling in buoyancy space. The downwelling above this corresponds to stable stratification and a strong decrease in diffusivity with height above bottom.

Above the downwelling, notice that there is largely weak upwelling in the interior; this is because the vertical diffusivity is at its background value of 5×10^{-5} m^2 s^{-1} (unenhanced by KPP), and variations in buoyancy flux are solely due to an increase in stratification with height. The labelled neutral density contours demonstrate that, at this latitude, densities below 28.16 kg m^{-3} have intersections with topography, and therefore experience some topographically enhanced upwelling. To formalise the importance of the topographic upwelling and downwelling of each density class, we now calculate the domain-wide water mass transformation, as defined by equation (4).

Figure 7b shows water mass transformation averaged over 30 days, using daily average κ and N^2 fields. There are large contributions from both total upwelling (red) and downwelling (blue), which are split by whether they occur within 250 m of topography (boundary, lighter colours) or above this (interior, darker colours). It is clear that the majority of both up- and downwelling occurs within 250 m of topography, as is expected from figure 7a. The net transformation (the sum of upwelling and downwelling) is shown in green dashed, with the white shading indicating one standard deviation of the 30-day time series. Despite temporal variation (to be discussed later), it is clear that densities greater than 28.19 kg m^{-3} (corresponding to SPDW and WSDW) upwell, whereas densities between 28.19 and 28.15 kg m^{-3} (corresponding to lighter LCDW) downwell. Lighter (interior) density classes experience much less transformation, since they intersect less with topography and therefore do not experience enhanced diffusivities.

The result that the densest waters upwell close to topography, with downwelling occurring above, is, to our knowledge, the first verification of the upwelling/downwelling hypothesis in a realistic, submesoscale- and internal wave-resolving numerical model with online diffusivity parameterization. A recent study by Drake et al. (2022) resolved the three-dimensional physical processes leading to diapycnal upwelling, downwelling, and re-stratification near topography in a quasi-realistic simulation of a canyon in the Brazil Basin. Using an idealised flow with an initially uniform stratification and a realistic topography, they showed that an imposed observationally-based exponential diffusivity profile led to near-boundary diapycnal upwelling by a three-dimensional eddying submesoscale flow. Our work, although in a different region, therefore provides a step forwards in realism by resolving the larger-scale context of the flow (such as realistic large- and mesoscale currents, non-uniform stratification, and spatially variable water masses), and by using an online diffusivity parameterization to represent the processes that cause mixing. However, we necessarily compromise on resolution of the bottom boundary layer, and our results must therefore be taken with some caution.

By calculating the water mass transformation in the absence of the bottom grid-cell, it becomes clear that much of the upwelling of the heaviest density classes is happening there, where the insulating boundary condition effectively imposes upwelling. Indeed, several studies have calculated water mass transformations globally using climatologies and estimates of mixing from various sources, by implicitly ensuring boundary upwelling in the bottom grid cell (at any vertical resolution) due to the insulating boundary condition at topography (De Lavergne et al., 2016; Ferrari et al., 2016; Mashayek, Salehipour, et al., 2017; Cimoli et al., 2019).

The grey dashed line in figure 7b shows the net water mass transformation without the bottom grid-cell. There remains a small amount of upwelling of the densest waters, but downwelling largely dominates. This indicates that we are not sufficiently resolving the bottom boundary layer to fully capture the upwelling/downwelling boundary with 25 m vertical resolution. This is consistent with one-dimensional idealised boundary layer solutions for sloping bathymetry with parameters similar to ours, which suggest that diapycnal upwelling occurs in a layer of height O(50 m) (Holmes & McDougall, 2020). Similarly, the quasi-realistic Brazil Basin simulations of Drake et al. (2022) with 6 m vertical resolution demonstrated marginally resolved diapycnal upwelling in a bottom boundary layer of O(10) m.

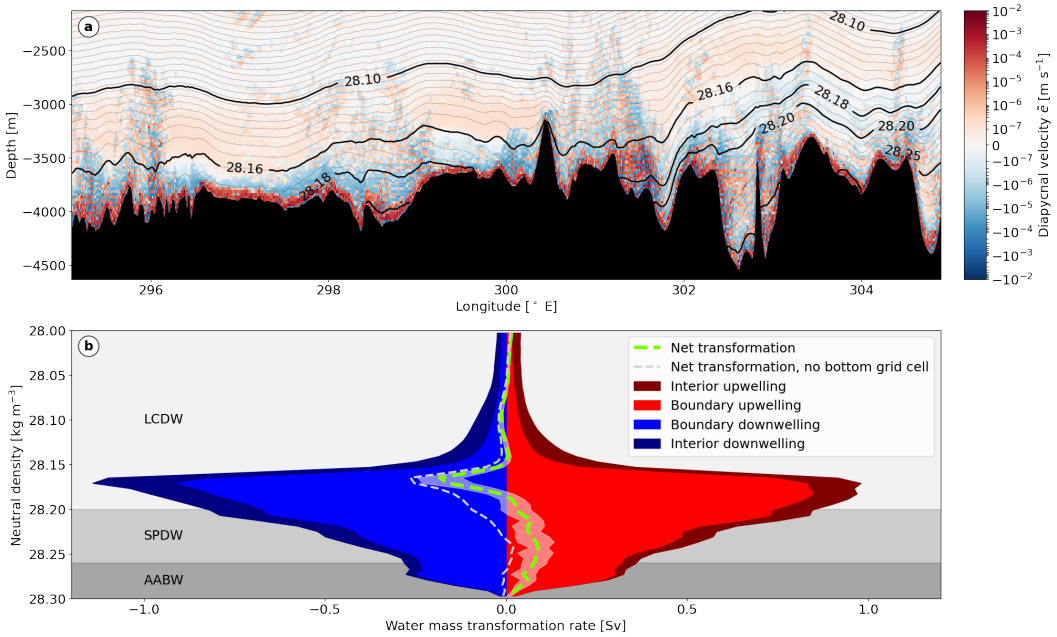

Figure 7. (a) 30-day average diapycnal velocity at -57° N, computed as in equation (3), with neutral density contours. (b) Water mass transformation calculated using equation (4) from daily average density and vertical diffusivity fields, and averaged over 30 days. Interior and boundary contributions are defined by below/above 250 m above bottom. White shading around the net transformation (green dashed) indicates ± 1 standard deviation of the 30-day time series. The white dashed line shows net transformation when the bottom grid-cell is excluded from the calculation.

However, we do find that there is considerable upwelling outside of the bottom grid-cell, as is clear from figure 7a, even though it is compensated by downwelling elsewhere. This gives us confidence that some realistic processes inducing upwelling of the densest waters are represented in this model. Furthermore, the daily averaged fields used to construct figure 7b may filter out some of the higher-frequency processes generating upwelling near the boundary, which we now investigate further.

6.3 Temporal variability

There is considerable temporal variability of the water mass transformation over the 30-day time period analysed, and there is therefore sensitivity to the frequency of output fields used. In figure 8a, we show the net transformation rate over the final 10 days of the simulation, calculated using hourly average fields, daily average fields, and 10-day average fields. The corresponding results without the bottom grid-cell are shown as dashed lines of the same colour.

In each case, upwelling occurs at densities in excess of 28.19 kg m^{-3}, with downwelling above. This result is thus robust to the frequency of fields used. However, when using hourly output (and therefore most accurately representing transformation rate over the 10-day period), we find that there is significant upwelling of dense waters even when the bottom grid-cell is not included. This suggests that higher-frequency dynamics, such as transient boundary overturns, are key in upwelling dense waters in the bottom few hundred metres.

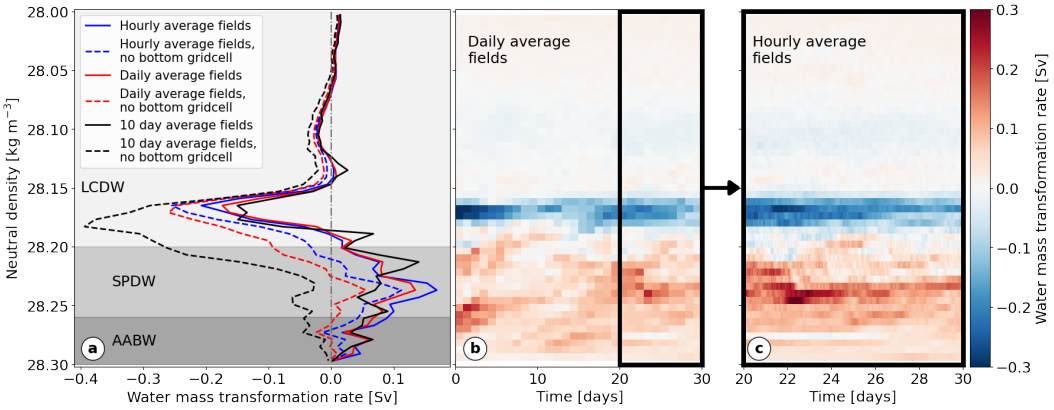

Figure 8. (a) Net water mass transformation rate (corresponding to green dashed line in figure 7a) as an average over 10 days, using fields saved at different frequencies. Dashed lines represent transformation rate with bottom grid-cell excluded. (b) Temporal variability of net water mass transformation rate over 30 days using daily average fields. (c) Temporal variability of net water mass transformation rate over 10 days (corresponding to final 10 days of (b)) from hourly output fields.

The temporal variability of transformation rate is shown using daily averages over 30 days in figure 8b, and using hourly averages over the final 10 days in figure 8c. Upwelling below the 28.19 kg m^{-3} surface, and downwelling above it, are a feature at all times. However, there is significant variability in the strength of the upwelling. In particular, a high-upwelling event occurs at approximately 22 days, at densities between 28.22 and 28.25 kg m^{-3}. It is very likely that this event corresponds to the high topographic mixing caused by the AABW overflow of the West Scotia Ridge demonstrated in figure 6, which occurs at this time. This suggests that the transformation of AABW into lighter water classes is inherently linked to the dynamics and location of the interface across which it must mix.

7 Sensitivity to model diffusivity

The model-based diffusivity shown in figures 5 and 6, while rooted in sound physical concepts (i.e. shear-induced and convective mixing as parameterized through KPP), is clearly insufficient. The diffusivity maps show mixing in the close vicinity of the seafloor (the last few grid points of the model) and lack much information in the interior, where diffusivity is simply set to a low background value. Observational estimates of mixing, however, show much more continuous variations in diffusivity as one approaches the seafloor (e.g., see Waterhouse et al. (2014)), implying intermittent turbulence in the ocean interior. The shortcoming of KPP is expected, as an important contribution of this work is permitting processes (in the model) that contribute to abyssal mixing. Only further study of such processes, which inevitably will require fully resolving them in even higher-resolution process-study models, will enhance our physical understanding sufficiently to allow for new parameterizations or for their integration into existing frameworks such as the KPP.

Since the nature of the simplistic KPP output has a bearing on the upwelling-downwelling patterns and their corresponding net water mass transformation rates discussed in figures 7 and 8, here we also consider an alternate diffusivity parameterization. Figure 9 shows the application of a recently developed machine learning (ML) based diffusivity parameterization (Mashayek, Reynard, et al., 2022), which was shown to be rather skillful in the Drake Passage region, to an hourly-average 'snapshot' from the simulation. The ML diffusivity

map shows a broader distribution of mixing above the seafloor (as opposed to the bottom-focused diffusivity from KPP) which simply reflects the fact that the ML-parameterization was trained on microstructure-based profiles exhibiting a gentler transition from interior to boundary mixing. The patterns emerging from the ML estimates are physically sensible, as they correspond to mixing by overturns along the seafloor (as discussed before and 'felt' by the KPP), but also above the seafloor due to breaking of lee waves and shearing of the sharp interfacial dynamics (neither captured by the KPP). Figure 1c confirms the good fit of the ML diffusivity estimate to observations when averaged with reference to height above bottom, and also shows that it gives a lower diffusivity at all heights above bottom than KPP.

The net transformation rates calculated from the KPP-based and ML-based diffusivities have significant differences (figures 9c,d), although the ML parameterisation still captures upwelling of the densest waters (AABW and SPDW). As discussed earlier, the rate at which the interior mixing increases towards the seafloor, and then decreases in the bottom boundary layer to yield a net zero flux at the solid boundary, controls the rate of boundary upwelling and the overlying downwelling. Thus, the smoother transition in mixing from interior to the seafloor in the ML-based estimate results in significantly weaker downwelling and upwelling rates.

Neither the KPP nor the ML representations of mixing are ideal. The former is based on physical principles, but lacks complexity due to our incomplete understanding of the processes that contribute to mixing. The latter is rooted in observations and physical understanding, but can certainly improve significantly as: (i) more observational data become available for training ML models, and (ii) more physical understanding is entrained in training the ML algorithms. Nevertheless, together, the two estimates (figures 9a,b) provide a bound on the uncertainty involved in estimates of mixing in even a realistic model of such unprecedented high resolution as ours. Thus, figure 9 helps us make two important points. First, it highlights the need for development of better mixing parameterizations in order to confidently determine the mixing of deep water masses and their net upwelling rates. Second, while at early stages, ML-based estimates, once connected with physical understanding, can prove a valuable tool for constraining deep-ocean mixing and meridional overturning.

The differences between the KPP and ML parameterizations do not impact the main messages of this paper, which are that (i) the dynamical interaction of water mass interfaces with topography is itself a source of instability and mixing in the deep ocean, (ii) the presence of these interfaces in the abyssal ocean can modify the nature of other topographic processes such as lee waves, and (iii) that small-scale, temporally variable, topographic interaction processes within a few hundred metres of the seafloor result in upwelling of AABW.

8 Discussion

We have used a high-resolution, realistic simulation to investigate the processes governing turbulent diapycnal mixing and water mass transformation of dense AABW as it flows through the Drake Passage. In addition to confirming the importance of known contributors to regional abyssal mixing (such as lee waves), we have also identified for the first time the dynamical role of highly stratified water mass interfaces in generating turbulence in the deep ocean.

Observational studies have previously reported the presence of highly stratified interfaces between deep water masses in several locations globally, including the Drake Passage (Sievers & Nowlin, 1984; Meredith et al., 2013; Reid et al., 1977). We have identified these stratified interfaces in further observations in the area as well as in our simulation, where the interfaces correspond to boundaries between deep CDW varieties (LCDW and SPDW) and the regional AABW (WSDW). The interfaces exhibit strong variability in time and space, and are often horizontally tilted by topography and mesoscale eddies.

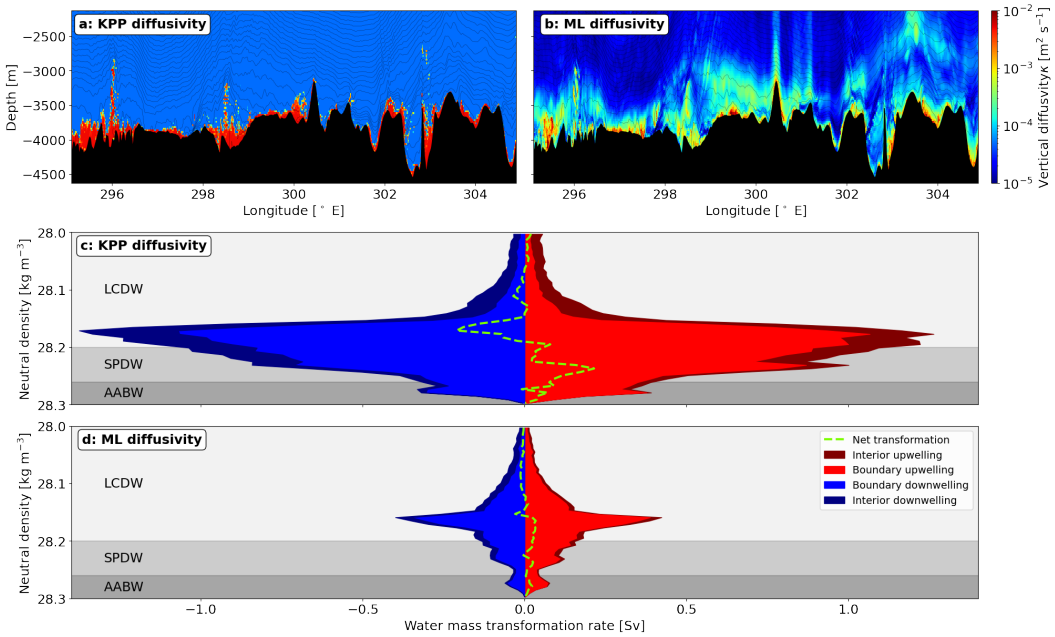

Figure 9. (a) Hourly average online KPP vertical diffusivity on day 94 (equivalent to figure 5b). (b) Offline diffusivity calculated from simulation fields using algorithm learnt from global observational turbulence data (Mashayek, Reynard, et al., 2022). (c) Water mass transformation calculated over the full domain from KPP diffusivity for an hourly average on day 94 (c.f. figure 7b). (d) As in (c), calculated using machine learning-based diffusivity shown in (b).

We conclude, based on our simulation, that these interfaces may play an important role in the upwelling of AABW by boosting topographic mixing processes in the deep ocean. We have identified several dynamical impacts of the interfaces: (i) creation of vertical shear in the deep ocean by geostrophic adjustment of tilted interfaces; (ii) interaction of strong horizontal buoyancy gradients with topography to induce convective overturning; and (iii) impact on the generation, propagation and breaking of lee waves.

The evidence presented here for the existence of such water mass interfaces at depth and their impact on abyssal dynamics raises important questions that will require further study. We conjectured that the maintenance of the interfaces' high stratification may be linked to frontogenetic processes in the deep ocean, but this should be examined in detail. Further, the occurrence and relevance of these interfaces over the Southern Ocean and globally should be investigated. Unfortunately, even state-of-the-art resolution global ocean models, such as the 1/48° LLC4320 global simulation (Rocha et al., 2016; Su et al., 2018) do not have sufficient vertical resolution at depth to adequately capture water mass interfaces. We found no evidence of stratified interfaces in the LLC4320 model in the Drake Passage, likely owing to the resolution at 4000 m depth being $\sim$ 200 m. If, as suggested here, water mass interfaces impact topographic turbulence and lee wave generation and breaking, this effect would be extremely challenging to account for in mixing parameterizations embedded in coarse models.

Using an online parameterization of diffusivity, we were able to link topographic mixing processes to quantification of water mass transformation in the Drake Passage. Waters denser than 28.19, corresponding to SPDW and WSDW, were found to experience net upwelling, whereas the LCDW above experiences net downwelling. We proposed that an

episode of strong AABW upwelling in the simulation was elicited by an overflow of dense AABW over a large topographic ridge system, linking the dynamics of the interface (both in terms of its location and effect on mixing) to cross-interface upwelling.

Our work constitutes a first realistic demonstration of how resolved submesoscale and internal wave-driven mixing processes induce boundary upwelling of deep waters, as predicted by the recently put forward upwelling/downwelling paradigm (De Lavergne et al., 2016; Ferrari et al., 2016; McDougall & Ferrari, 2017). However, still higher vertical resolution on the order of metres is needed to satisfactorily resolve upwelling in the bottom boundary layer (Drake et al., 2022). We also demonstrated the need for hourly temporal resolution to capture the water mass transformation correctly, especially outside of the bottom grid-cell. This implies that that the processes driving diapycnal upwelling are highly temporally variable. Given the demonstrated importance of realistic topography, stratification and flow, and of metre-scale boundary layer dynamics in quantifying AABW transformation, unprecedented model resolution would be required to fully capture the wide range of scales of this problem.

Through comparison of our online KPP diffusivity parameterization and resulting water mass transformation with results based on a recent machine learning estimate of diffusivity, we showed that considerable uncertainties remain in the vertical diffusivity representation of abyssal processes. This brings about a limited ability of even high resolution regional models to adequately constrain the transformation rate of abyssal waters. Knowledge of this transformation rate is essential to our understanding of the ocean's overturning circulation and oceanic transport and storage of climatically important tracers. Resolving these outstanding questions in the future will require a multifaceted approach of higher-resolution model process studies, innovative applications of machine learning, and more extensive abyssal observations in different turbulent regimes.

Appendix A Drake Passage Model Setup

The simulation is performed at 0.01° horizontal resolution using the MITgcm (Marshall et al., 1997) in hydrostatic configuration. There are 225 vertical levels, with resolution dz varying smoothly from $dz = 10$ m at the surface to $dz = 25$ m at 600 m depth, $dz = 25$ m between 600 and 4,555 m depth, and varying smoothly from $dz = 25$ m to 62 m at the maximum depth of 5,660 m. Partial cells are used at topography with a minimum height of 10 m. The timestep is 24 s.

The simulation is forced at the open boundaries by the OCCA state estimate (Forget, 2010) as described in the main text. The nonlinear free surface is forced by near surface air temperature, wind speed, precipitation, humidity, long and short wave radiation from the ECMWF ERA-Interim reanalysis product (Simmons et al., 2006). The model does not include tides. The topography is interpolated from the Smith and Sandwell (1997) v15.1 1 min bathymetric product, and contains some areas of multibeam topography alongside satellite altimetry derived estimates of topography.

The bottom boundary condition is no-slip, which is implemented in the MITgcm through an extra drag term in the bottom grid cell. In addition, we use a quadratic drag with a coefficient of 2.5×10^{-3} to represent unresolved small scale topography; see MITgcm documentation (https://mitgcm.readthedocs.io) and Legg et al. (2006) for details.

Horizontal viscosity is implemented with the biharmonic Leith scheme with a coefficient of 2 (Fox-Kemper & Menemenlis, 2008; Leith, 1996). Background vertical viscosity and diffusivity of temperature and salinity are set at 5×10^{-5} m^2 s^{-1}. The KPP parameterization (Large et al., 1994) enhances vertical diffusivity (and viscosity) in the interior according to criteria for shear and convective instability. The critical Richardson number for onset of shear instability is 1/3.

Open Research

All software and processed data required to enable the reader to reproduce our results are published via Zenodo at doi.org/10.5281/zenodo.7410908 (Baker et al., 2022). The MITgcm (Marshall et al., 1997) is documented at https://mitgcm.readthedocs.io and available at doi.org/10.5281/zenodo.1409237 (Campin et al., 2019).

Observational CTD data along the SR1b section, collected by the ACCLAIM project and used in figures 1e and 2, and CTD and ADCP data collected by the DIMES project used in figure 4 are available from bodc.ac.uk/data.

Conflict of Interest Statement

The authors have no conflicts of interest to declare.

Acknowledgments

L.B. was supported by the Centre for Doctoral Training in Mathematics of Planet Earth, UK EPSRC funded (Grant EP/L016613/1), and A.M. acknowledges funding from the NERC IRF fellowship grant NE/P018319/1. Computational resources provided by the Imperial College London Research Computing Service are gratefully acknowledged (https://doi.org/10.14469/hpc/2232).

References

Alford, M. H., Girton, J. B., Voet, G., Carter, G. S., Mickett, J. B., & Klymak, J. M. (2013). Turbulent mixing and hydraulic control of abyssal water in the Samoan Passage. *Geophys. Res. Lett.*, *40*(17), 4668–4674. doi: 10.1002/grl.50684

Armi, L., & Mayr, G. J. (2015). Virtual and real topography for flows across mountain ranges. *J. Appl. Meteorol. Climatol.*, *54*(4), 723–731. doi: 10.1175/JAMC-D-14-0231.1

Baines, P. G. (1995). *Topographic effects in stratified flows.* Cambridge: Cambridge University Press.

Baker, L. E., & Mashayek, A. (2021). Surface reflection of bottom generated oceanic lee waves. *J. Fluid Mech.*, *924*(A17), 1–42. doi: 10.1017/jfm.2021.627

Baker, L. E., & Mashayek, A. (2022). The Impact of Representations of Realistic Topography on Parameterized Oceanic Lee Wave Energy Flux. *J. Geophys. Res. Ocean.*, 1–34. doi: 10.1029/2022JC018995

Baker, L. E., Mashayek, A., & Naveira-Garabato, A. C. (2022). *Enhanced upwelling of Antarctic Bottom Water by topographic interaction of water mass interfaces [Software and Dataset].* Zenodo. doi: 10.5281/zenodo.7410908

Callies, J. (2018). Restratification of abyssal mixing layers by submesoscale baroclinic eddies. *J. Phys. Oceanogr.*, *48*(9), 1995–2010. doi: 10.1175/JPO-D-18-0082.1

Campin, J.-M., Heimbach, P., Losch, M., Forget, G., Edhill3, Adcroft, A., ... Dussin, R. (2019). *MITgcm/MITgcm: checkpoint67g [Software].* Zenodo. doi: 10.5281/zenodo.1409237

Caulfield, C. (2021). Layering, Instabilities, and Mixing in Turbulent Stratified Flows. *Annu. Rev. Fluid Mech.*, *53*(1). doi: 10.1146/annurev-fluid-042320-100458

Cimoli, L., Caulfield, C. c. P., Johnson, H. L., Marshall, D. P., Mashayek, A., Naveira Garabato, A. C., & Vic, C. (2019). Sensitivity of Deep Ocean Mixing to Local Internal Tide Breaking and Mixing Efficiency. *Geophys. Res. Lett.*, *46*(24), 14622–14633. doi: 10.1029/2019GL085056

Cusack, J. M., Naveira Garabato, A. C., Smeed, D. A., & Girton, J. B. (2017). Observation of a Large Lee Wave in the Drake Passage. *J. Phys. Oceanogr.*, *47*(4), 793–810. doi: 10.1175/JPO-D-16-0153.1

De Lavergne, C., Madec, G., Le Sommer, J., Nurser, A. J., & Naveira Garabato, A. C. (2016). On the consumption of Antarctic Bottom Water in the abyssal ocean. *J. Phys. Oceanogr.*, *46*(2), 635–661. doi: 10.1175/JPO-D-14-0201.1

Drake, H. F., Ferrari, R., & Callies, J. (2020). Abyssal circulation driven by near-boundary mixing: Water mass transformations and interior stratification. *J. Phys. Oceanogr.*, *50*(8), 2203–2226. doi: 10.1175/JPO-D-19-0313.1

Drake, H. F., Ruan, X., Callies, J., Ogden, K., Thurnherr, A. M., & Ferrari, R. (2022). Dynamics of eddying abyssal mixing layers over sloping rough topography. *J. Phys. Oceanogr.*. doi: 10.1175/jpo-d-22-0009.1

Durran, D. R. (1986). Another Look at Downslope Windstorms. Part I: The Development of Analogs to Supercritical Flow in an Infinitely Deep, Continuously Stratified Fluid. *J. Atmos. Sci.*, *43*(21), 2527–2543. doi: 10.1175/1520-0469(1986)043⟨2527:ALADWP⟩2.0.CO;2

Emile-Geay, J., & Madec, G. (2009). Geothermal heating, diapycnal mixing and the abyssal circulation. *Ocean Sci.*, *5*(2), 203–217. doi: 10.5194/os-5-203-2009

Ferrari, R., Mashayek, A., McDougall, T. J., Nikurashin, M., & Campin, J. M. (2016). Turning ocean mixing upside down. *J. Phys. Oceanogr.*, *46*(7), 2239–2261. doi: 10.1175/JPO-D-15-0244.1

Forget, G. (2010, jun). Mapping ocean observations in a dynamical framework: A 2004-06 ocean atlas. *J. Phys. Oceanogr.*, *40*(6), 1201–1221. doi: 10.1175/2009JPO4043.1

Fox-Kemper, B., & Menemenlis, D. (2008). Can large eddy simulation techniques improve mesoscale rich ocean models? *Geophys. Monogr. Ser.*, *177*, 319–337. doi: 10.1029/177GM19

Garrett, C., MacCready, P., & Rhines, P. (1993). Boundary mixing and arrested Ekman layers: rotating stratified flow near a sloping boundary. *Annu. Rev. Fluid Mech.*. doi: 10.1146/annurev.fluid.25.1.291

Gregg, M., D'Asaro, E., Riley, J., & Kunze, E. (2018). Mixing Efficiency in the Ocean. *Ann. Rev. Mar. Sci.*, *10*(1), 443–473. doi: 10.1146/annurev-marine-121916-063643

Gutierrez-Villanueva, M. O., Chereskin, T. K., Sprintall, J., & Goff, J. A. (2022). Turbulent Mixing and Lee-Wave Radiation in Drake Passage: Sensitivity to Topography. *J. Geophys. Res. Ocean.*, *127*(5), 1–25. doi: 10.1029/2021jc018103

Holmes, R. M., & McDougall, T. J. (2020). Diapycnal transport near a sloping bottom boundary. *J. Phys. Oceanogr.*, *50*(11), 3253–3266. doi: 10.1175/JPO-D-20-0066.1

Hoskins, B. J. (1982). The mathematical theory of frontogenesis. *Annu. Rev. fluid Mech. Vol. 14*, 131–151. doi: 10.1146/annurev.fl.14.010182.001023

Howard, L. (1961). Note on a paper of John W. Miles. *J. Fluid Mech.*, *10*(4), 509–512. doi: 10.1017/S0022112061000317

Jackett, D. R., & Mcdougall, T. J. (1997). A neutral density variable for the world's oceans. *J. Phys. Oceanogr.*, *27*(2), 237–263. doi: 10.1175/1520-0485(1997)027⟨0237:ANDVFT⟩2.0.CO;2

Jagannathan, A., Winters, K. B., & Armi, L. (2020). The effect of a strong density step on blocked stratified flow over topography. *J. Fluid Mech.*, *889*. doi: 10.1017/jfm.2020.87

Johnson, G. C. (2008). Quantifying Antarctic Bottom Water and North Atlantic Deep Water volumes. *J. Geophys. Res. Ocean.*, *113*(5), 1–13. doi: 10.1029/2007JC004477

Klemp, J. B., & Lilly, D. K. (1975). The dynamics of wave-induced downslope winds. *J. Atmos. Sci.*, *32*. doi: 10.1175/1520-0469(1975)032⟨0320:TDOWID⟩2.0.CO;2

Klymak, J. M. (2018). Nonpropagating form drag and turbulence due to stratified flow over large-scale Abyssal Hill Topography. *J. Phys. Oceanogr.*, *48*(10), 2383–2395. doi: 10.1175/JPO-D-17-0225.1

Klymak, J. M., Balwada, D., Garabato, A. N., & Abernathey, R. (2021). Parameterizing Nonpropagating Form Drag over Rough Bathymetry. *J. Phys. Oceanogr.*, *51*(5), 1489–1501. doi: 10.1175/jpo-d-20-0112.1

Kunze, E., & Lien, R.-C. (2019). Energy Sinks for Lee Waves in Shear Flow. *J. Phys. Oceanogr.*, 2851–2865. doi: 10.1175/jpo-d-19-0052.1

Large, W. G., McWilliams, J. C., & Doney, S. C. (1994). Oceanic vertical mixing: A review and a model with a nonlocal boundary layer parameterization. *Rev. Geophys.*, *32*(4), 363–403. doi: 10.1029/94RG01872

Ledwell, J. R., Montgomery, E. T., Polzin, K. L., St. Laurent, L. C., Schmitt, R. W., & Toole, J. M. (2000). Evidence for enhanced mixing over rough topography in the abyssal ocean. *Nature*, *403*, 179–182. doi: 10.1038/35003164

Legg, S. (2021). Mixing by Oceanic Lee Waves. *Annu. Rev. Fluid Mech.*, *53*, 173–201. doi: 10.1146/annurev-fluid-051220-043904

Legg, S., Hallberg, R. W., & Girton, J. B. (2006). Comparison of entrainment in overflows simulated by z-coordinate, isopycnal and non-hydrostatic models. *Ocean Model.*, *11*(1-2), 69–97. doi: 10.1016/j.ocemod.2004.11.006

Legg, S., & Klymak, J. (2008). Internal Hydraulic Jumps and Overturning Generated by Tidal Flow over a Tall Steep Ridge. *J. Phys. Oceanogr.*, *38*, 1949–1964. doi: 10.1175/2008JPO3777.1

Leith, C. E. (1996). Stochastic models of chaotic systems. *Phys. D Nonlinear Phenom.*, *98*(2-4), 481–491. doi: 10.1016/0167-2789(96)00107-8

Liu, M., & Tanhua, T. (2021). Water masses in the Atlantic Ocean: Characteristics and distributions. *Ocean Sci.*, *17*(2), 463–486. doi: 10.5194/os-17-463-2021

Lumpkin, R., & Speer, K. (2007). Global ocean meridional overturning. *J. Phys. Oceanogr.*, *37*(10), 2550–2562. doi: 10.1175/JPO3130.1

MacCready, P., & Rhines, P. B. (1991). Buoyant inhibition of ekman transport on a slope and its effect on stratified spin-up. *J. Fluid Mech.*, *223*, 631–661. doi: 10.1017/S0022112091001581

Mackay, N., Ledwell, J. R., Messias, M. J., Naveira Garabato, A. C., Brearley, J. A., Meijers, A. J., ... Watson, A. J. (2018, apr). Diapycnal Mixing in the Southern Ocean Diagnosed Using the DIMES Tracer and Realistic Velocity Fields. *J. Geophys. Res. Ocean.*, *123*(4), 2615–2634. doi: 10.1002/2017JC013536

MacKinnon, J., Laurent, L. S., & Garabato, A. C. N. (2013). Diapycnal Mixing Processes in the Ocean Interior. In *Ocean circ. clim. a 21st century perspect.* (Vol. 103, pp. 159–183). Retrieved from `http://www.sciencedirect.com/science/article/pii/B9780123918512000076` doi: https://doi.org/10.1016/B978-0-12-391851-2.00007-6

MacKinnon, J. A., Zhao, Z., Whalen, C. B., Griffies, S. M., Sun, O. M., Barna, A., ... Norton, N. J. (2017). Climate Process Team on Internal Wave–Driven Ocean Mixing. *Bull. Am. Meteorol. Soc.*, *98*(11), 2429–2454. doi: 10.1175/bams-d-16-0030.1

Marshall, J., Adcroft, A., Hill, C., Perelman, L., & Heisey, C. (1997). A finite-volume, incompressible navier stokes model for, studies of the ocean on parallel computers. *J. Geophys. Res. C Ocean.*, *102*(C3), 5753–5766. doi: 10.1029/96JC02775

Marshall, J., & Speer, K. (2012). Closure of the meridional overturning circulation through Southern Ocean upwelling. *Nat. Geosci.*, *5*(3), 171–180. doi: 10.1038/ngeo1391

Mashayek, A., Baker, L. E., Cael, B. B., & Caulfield, C. P. (2022). A Marginal Stability Paradigm for Shear-Induced Diapycnal Turbulent Mixing in the Ocean. *Geophys. Res. Lett.*, *49*(2), 1–11. doi: 10.1029/2021GL095715

Mashayek, A., Caulfield, C. P., & Alford, M. H. (2021). Goldilocks mixing in oceanic shear-induced turbulent overturns. *J. Fluid Mech.*, *928*, 1–32. doi: 10.1017/jfm.2021.740

Mashayek, A., Ferrari, R., Merrifield, S., Ledwell, J. R., St Laurent, L., & Garabato, A. N. (2017). Topographic enhancement of vertical turbulent mixing in the Southern Ocean. *Nat. Commun.*, *8*, 1–12. doi: 10.1038/ncomms14197

Mashayek, A., Ferrari, R., Vettoretti, G., & Peltier, W. R. (2013). The role of the geothermal heat flux in driving the abyssal ocean circulation. *Geophys. Res. Lett.*, *40*(12), 3144–3149. doi: 10.1002/grl.50640

Mashayek, A., Reynard, N., Zhai, F., Srinivasan, K., Jelley, A., Naveira Garabato, A., & Caulfield, C. P. (2022). Deep Ocean Learning of Small Scale Turbulence. *Geophys. Res. Lett.*, *49*(15), 1–9. doi: 10.1029/2022GL098039

Mashayek, A., Salehipour, H., Bouffard, D., Caulfield, C. P., Ferrari, R., Nikurashin, M., ... Caulfield, C. P. (2017). Efficiency of turbulent mixing in the abyssal ocean circulation.

Geophys. Res. Lett., *44*(12), 6296–6306. doi: 10.1002/2016gl072452

McDougall, T. J., & Ferrari, R. (2017). Abyssal upwelling and downwelling driven by near-boundary mixing. *J. Phys. Oceanogr.*, *47*(2), 261–283. doi: 10.1175/JPO-D-16-0082.1

McWilliams, J. C. (2021). Oceanic Frontogenesis. *Ann. Rev. Mar. Sci.*, *13*, 227–253. doi: 10.1146/annurev-marine-032320-120725

Meredith, M. P., Brown, P. J., Naveira Garabato, A. C., Jullion, L., Venables, H. J., & Messias, M. J. (2013). Dense bottom layers in the Scotia Sea, Southern Ocean: Creation, lifespan, and destruction. *Geophys. Res. Lett.*, *40*(5), 933–936. doi: 10.1002/grl.50260

Meredith, M. P., & Naveira Garabato, A. C. (2021). *Ocean Mixing*. Elsevier. doi: 10.1016/C2019-0-03674-6

Merrifield, S. T., Laurent, L. S., Owens, B., Thurnherr, A. M., & Toole, J. M. (2016). Enhanced diapycnal diffusivity in intrusive regions of the Drake passage. *J. Phys. Oceanogr.*, *46*(4), 1309–1321. doi: 10.1175/JPO-D-15-0068.1

Miles, J. W. (1961). On the stability of heterogeneous shear flows. *J. Fluid Mech.*, *10*(4), 496–508. doi: 10.1017/S0022112061000305

Moum, J. N. (2021). Variations in Ocean Mixing from Seconds to Years. *Ann. Rev. Mar. Sci.*, *13*, 201–226. doi: 10.1146/annurev-marine-031920-122846

Munk, W., & Wunsch, C. (1998). Abyssal recipes II Energetics of tidal and wind mixing. *Deep. Res.*, *I*(45), 1977–2010. doi: 10.1016/S0967-0637(98)00070-3

Naveira Garabato, A., Polzin, K., King, B., Heywood, K., & Visbeck, M. (2004). Widespread Intense Turbulent Mixing in the Southern Ocean. *Science (80-.).*, *303*(January), 210–213. doi: 10.1126/science.1090929

Naveira Garabato, A. C., Frajka-Williams, E. E., Spingys, C. P., Legg, S., Polzin, K. L., Forryan, A., ... Meredith, M. P. (2019). Rapid mixing and exchange of deep-ocean waters in an abyssal boundary current. *Proc. Natl. Acad. Sci. U. S. A.*, *116*(27), 13233–13238. doi: 10.1073/pnas.1904087116

Naveira Garabato, A. C., Heywood, K. J., & Stevens, D. P. (2002). Modification and pathways of Southern Ocean Deep Waters in the Scotia Sea. *Deep. Res. I*, *49*, 681–705. doi: 10.1016/S0967-0637(01)00071-1

Naveira Garabato, A. C., McDonagh, E. L., Stevens, D. P., Heywood, K. J., & Sanders, R. J. (2002). On the export of Antarctic Bottom Water from the Weddell Sea. *Deep. Res. Part II Top. Stud. Oceanogr.*, *49*(21), 4715–4742. doi: 10.1016/S0967-0645(02)00156-X

Naveira Garabato, A. C., Williams, A. P., & Bacon, S. (2014). The three-dimensional overturning circulation of the Southern Ocean during the WOCE era. *Prog. Oceanogr.*, *120*, 41–78. doi: 10.1016/j.pocean.2013.07.018

Nikurashin, M., & Ferrari, R. (2010). Radiation and Dissipation of Internal Waves Generated by Geostrophic Motions Impinging on Small-Scale Topography: Application to the Southern Ocean. *J. Phys. Oceanogr.*, *40*(9), 2025–2042. doi: 10.1175/2010jpo4315.1

Nikurashin, M., & Ferrari, R. (2011). Global energy conversion rate from geostrophic flows into internal lee waves in the deep ocean. *Geophys. Res. Lett.*, *38*(8), 1–6. doi: 10.1029/2011GL046576

Osborn, T. R. (1980). *Estimates of the Local Rate of Vertical Diffusion from Dissipation Measurements* (Vol. 10) (No. 1). doi: 10.1175/1520-0485(1980)010⟨0083:eotlro⟩2.0.co;2

Peltier, W., & Clark, T. (1979). The Evolution and Stability of Finite-Amplitude Mountain Waves. Part II: Surface Wave Drag and Severe Downslope Windstorms. *J. Atmos. Sci.*, *36*(9), 1498–1529. doi: 10.1175/1520-0469(1980)037⟨2119:COEASO⟩2.0.CO;2

Polzin, K. L., & McDougall, T. J. (2022). Mixing at the ocean's bottom boundary. In M. P. Meredith & A. C. Naveira Garabato (Eds.), *Ocean mix.* (pp. 145–180). Elsevier. doi: 10.1016/b978-0-12-821512-8.00014-1

Polzin, K. L., Toole, J. M., Ledwell, J. R., & Schmitt, R. W. (1997). Spatial variability of turbulent mixing in the abyssal ocean. *Science (80-.).*, *276*(5309), 93–96. doi: 10.1126/science.276.5309.93

Purkey, S. G., Smethie, W. M., Gebbie, G., Gordon, A. L., Sonnerup, R. E., Warner, M. J., & Bullister, J. L. (2018). A synoptic view of the ventilation and circulation of antarctic bottom water from chlorofluorocarbons and natural tracers. *Ann. Rev. Mar. Sci.*, *10*(September), 503–527. doi: 10.1146/annurev-marine-121916-063414

Rae, J. W., Burke, A., Robinson, L. F., Adkins, J. F., Chen, T., Cole, C., ... Taylor, B. J. (2018). CO2 storage and release in the deep Southern Ocean on millennial to centennial timescales. *Nature*, *562*(7728), 569–573. doi: 10.1038/s41586-018-0614-0

Reid, J., Nowlin, W., & Patzert, W. (1977). On the Characteristics and Circulation of the Southwestern Atlantic Ocean. *J. Phys. Oceanogr.*, *7*, 62–91. doi: 10.1175/1520-0485(1977)007⟨0062:OTCACO⟩2.0.CO;2

Rocha, C. B., Chereskin, T. K., Gille, S. T., & Menemenlis, D. (2016). Mesoscale to submesoscale wavenumber spectra in Drake Passage. *J. Phys. Oceanogr.*, *46*(2), 601–620. doi: 10.1175/JPO-D-15-0087.1

Ruan, X., Thompson, A. F., & Taylor, J. R. (2019). The evolution and arrest of a turbulent stratified oceanic bottom boundary layer over a slope: Downslope regime. *J. Phys. Oceanogr.*, *49*(2), 469–487. doi: 10.1175/JPO-D-18-0079.1

Ruan, X., Thompson, A. F., & Taylor, J. R. (2021). The evolution and arrest of a turbulent stratified oceanic bottom boundary layer over a slope: Upslope regime and pv dynamics. *J. Phys. Oceanogr.*, *51*(4), 1077–1089. doi: 10.1175/JPO-D-20-0168.1

Sarkar, S., & Scotti, A. (2017). From Topographic Internal Gravity Waves to Turbulence. *Annu. Rev. Fluid Mech.*, *49*(1), 195–220. doi: 10.1146/annurev-fluid-010816-060013

Scott, R. B., Goff, J. A., Naveira Garabato, A. C., & Nurser, A. J. G. (2011). Global rate and spectral characteristics of internal gravity wave generation by geostrophic flow over topography. *J. Geophys. Res.*, *116*(C09029), 1–14. doi: 10.1029/2011JC007005

Sheen, K. L., Brearley, J. A., Naveira Garabato, A. C., Smeed, D. A., Waterman, S., Ledwell, J. R., ... Watson, A. J. (2013). Rates and mechanisms of turbulent dissipation and mixing in the Southern Ocean: Results from the Diapycnal and Isopycnal Mixing Experiment in the Southern Ocean (DIMES). *J. Geophys. Res. Ocean.*, *118*(6), 2774–2792. doi: 10.1002/jgrc.20217

Sheridan, P. F., & Vosper, S. B. (2006). A flow regime diagram for forecasting lee waves, rotors and downslope winds. *Meteorol. Appl.*, *13*(2), 179–195. doi: 10.1017/S1350482706002088

Siegelman, L., Klein, P., Rivière, P., Thompson, A. F., Torres, H. S., Flexas, M., & Menemenlis, D. (2020). Enhanced upward heat transport at deep submesoscale ocean fronts. *Nat. Geosci.*, *13*(1), 50–55. doi: 10.1038/s41561-019-0489-1

Sievers, H. A., & Nowlin, W. D. (1984). The stratification and water masses at Drake Passage. *J. Geophys. Res.*, *89*(C6), 10489. doi: 10.1029/jc089ic06p10489

Simmons, A., Uppala, S., Dee, D., & Kobayashi, S. (2006). ERA-Interim: New ECMWF reanalysis products from 1989 onwards. *ECMWF Newsl.*, *110*, 25–35. doi: 10.21957/pocnex23c6

Skinner, L., Fallon, S., Waelbroeck, C., Michel, E., & Barker, S. (2010). Ventilation of the Deep Southern Ocean and Deglacial CO2 Rise. *Science (80-.).*, *328*, 1147–1152. doi: 10.1126/science.1183627

Smith, W. H., & Sandwell, D. T. (1997). Global sea floor topography from satellite altimetry and ship depth soundings. *Science (80-.).*, *277*(5334), 1956–1962. doi: 10.1126/science.277.5334.1956

Smyth, W. D. (2020). Marginal instability and the efficiency of ocean mixing. *J. Phys. Oceanogr.*, *50*(8), 2141–2150. doi: 10.1175/JPO-D-20-0083.1

Solodoch, A., Stewart, A. L., Hogg, A. M. C., Morrison, A. K., Kiss, A. E., Thompson, A. F., ... Cimoli, L. (2022). How Does Antarctic Bottom Water Cross the Southern Ocean? *Geophys. Res. Lett.*, *49*(7), 1–11. doi: 10.1029/2021GL097211

Spingys, C. P., Naveira Garabato, A. C., Legg, S., Polzin, K. L., Abrahamsen, E. P., Buckingham, C. E., ... Frajka-Williams, E. E. (2021, jan). Mixing and Transformation in a Deep Western Boundary Current: A Case Study. *J. Phys. Oceanogr.*, *51*(4), 1205–1222. doi: 10.1175/jpo-d-20-0132.1

Srinivasan, K., McWilliams, J. C., Molemaker, M. J., & Barkan, R. (2019). Submesoscale Vortical Wakes in the Lee of Topography. *J. Phys. Oceanogr.*, *49*(7), 1949–1971. doi: 10.1175/jpo-d-18-0042.1

St. Laurent, L., Naveira Garabato, A. C., Ledwell, J. R., Thurnherr, A. M., Toole, J. M., & Watson, A. J. (2012). Turbulence and diapycnal mixing in drake passage. *J. Phys. Oceanogr.*, *42*(12), 2143–2152. doi: 10.1175/JPO-D-12-027.1

St. Laurent, L. C., Toole, J. M., & Schmitt, R. W. (2001). Buoyancy forcing by turbulence above rough topography in the abyssal Brazil Basin. *J. Phys. Oceanogr.*, *31*(12), 3476–3495. doi: 10.1175/1520-0485(2001)031⟨3476:BFBTAR⟩2.0.CO;2

Su, Z., Wang, J., Klein, P., Thompson, A. F., & Menemenlis, D. (2018). Ocean submesoscales as a key component of the global heat budget. *Nat. Commun.*, *9*(1), 1–8. doi: 10.1038/s41467-018-02983-w

Talley, L. D. (2013). Closure of the global overturning circulation through the Indian, Pacific, and southern oceans. *Oceanography*, *26*(1), 80–97. doi: 10.5670/oceanog.2013.07

Tamsitt, V., Drake, H. F., Morrison, A. K., Talley, L. D., Dufour, C. O., Gray, A. R., ... Weijer, W. (2017, dec). Spiraling pathways of global deep waters to the surface of the Southern Ocean. *Nat. Commun.*, *8*(1). doi: 10.1038/s41467-017-00197-0

Thomas, L. N., Taylor, J. R., Ferrari, R., & Joyce, T. M. (2013, jul). Symmetric instability in the Gulf Stream. *Deep. Res. Part II Top. Stud. Oceanogr.*, *91*, 96–110. doi: 10.1016/j.dsr2.2013.02.025

Thorpe, S. A., & Liu, Z. (2009). Marginal instability? *J. Phys. Oceanogr.*, *39*(9), 2373–2381. doi: 10.1175/2009JPO4153.1

Toggweiler, J. R. (1994). The Ocean's Overturning Circulation. *Phys. Today*, *47*(11), 45–50. doi: 10.1063/1.881425

Tomczak, M., & Large, D. G. B. (1989). Optimum multiparameter analysis of mixing in the thermocline of the eastern Indian Ocean. *J. Geophys. Res.*, *94*(C11), 16141. doi: 10.1029/jc094ic11p16141

Trossman, D. S., Arbic, B. K., Garner, S. T., Goff, J. A., Jayne, S. R., Metzger, E. J., & Wallcraft, A. J. (2013). Impact of parameterized lee wave drag on the energy budget of an eddying global ocean model. *Ocean Model.*, *72*, 119–142. doi: 10.1016/j.ocemod.2013.08.006

Tulloch, R., Ferrari, R., Jahn, O., Klocker, A., Lacasce, J., Ledwell, J. R., ... Watson, A. (2014). Direct estimate of lateral eddy diffusivity upstream of drake passage. *J. Phys. Oceanogr.*, *44*(10), 2593–2616. doi: 10.1175/JPO-D-13-0120.1

Voet, G., Alford, M. H., MacKinnon, J. A., & Nash, J. D. (2020). Topographic Form Drag on Tides and Low-Frequency Flow: Observations of Nonlinear Lee Waves over a Tall Submarine Ridge near Palau. *J. Phys. Oceanogr.*, 1489–1507. doi: 10.1175/jpo-d-19-0257.1

Vosper, S. B. (2004). Inversion effects on mountain lee waves. *Q. J. R. Meteorol. Soc.*, *130*(600 PART A), 1723–1748. doi: 10.1256/qj.03.63

Walin, G. (1982). On the relation between sea-surface heat flow and thermal circulation in the ocean. *Tellus*, *34*(2), 187–195. doi: 10.3402/tellusa.v34i2.10801

Waterhouse, A. F., Mackinnon, J. A., Nash, J. D., Alford, M. H., Kunze, E., Simmons, H. L., ... Lee, C. M. (2014). Global patterns of diapycnal mixing from measurements of the turbulent dissipation rate. *J. Phys. Oceanogr.*, *44*(7), 1854–1872. doi: 10.1175/JPO-D-13-0104.1

Waterman, S., Naveira Garabato, A. C., & Polzin, K. L. (2013). Internal waves and turbulence in the antarctic circumpolar current. *J. Phys. Oceanogr.*, *43*(2), 259–282. doi: 10.1175/JPO-D-11-0194.1

Waterman, S., Polzin, K. L., Garabato, A. C., Sheen, K. L., & Forryan, A. (2014). Suppression of internal wave breaking in the antarctic circumpolar current near topography. *J. Phys. Oceanogr.*, *44*(5), 1466–1492. doi: 10.1175/JPO-D-12-0154.1

Watson, A. J., Ledwell, J. R., Messias, M. J., King, B. A., Mackay, N., Meredith, M. P., ... Naveira Garabato, A. C. (2013). Rapid cross-density ocean mixing at mid-depths in the Drake Passage measured by tracer release. *Nature*, *501*(7467), 408–411. doi:

10.1038/nature12432

Wenegrat, J. O., & Thomas, L. N. (2020). Centrifugal and symmetric instability during Ekman adjustment of the bottom boundary layer. *J. Phys. Oceanogr.*, *50*, 1793–1812. doi: 10.1175/JPO-D-20-0027.1

Whalen, C. B., de Lavergne, C., Naveira Garabato, A. C., Klymak, J. M., MacKinnon, J. A., & Sheen, K. L. (2020). Internal wave-driven mixing: governing processes and consequences for climate. *Nat. Rev. Earth Environ.*, *1*(11), 606–621. doi: 10.1038/s43017-020-0097-z

Winters, K. B., & Armi, L. (2012). Hydraulic control of continuously stratified flow over an obstacle. *J. Fluid Mech.*, *700*, 502–513. doi: 10.1017/jfm.2012.157

Winters, K. B., & Armi, L. (2014). Topographic control of stratified flows: Upstream jets, blocking and isolating layers. *J. Fluid Mech.*, *753*, 80–103. doi: 10.1017/jfm.2014.363

Wunsch, C., & Ferrari, R. (2004). Vertical Mixing, Energy, and the General Circulation of the Oceans. *Annu. Rev. Fluid Mech.*, *36*(1), 281–314. doi: 10.1146/annurev.fluid.36.050802.122121

Zika, J. D., Sallee, J. B., Meijers, A. J., Naveira-Garabato, A. C., Watson, A. J., Messias, M. J., & King, B. A. (2020). Tracking the spread of a passive tracer through Southern Ocean water masses. *Ocean Sci.*, *16*(2), 323–336. doi: 10.5194/os-16-323-2020